batteries

MDPI

Review

A Review of Nb_2CT_x MXene: Synthesis, Properties and Applications

Guozhen Guan and Fengmei Guo *

Key Laboratory of Material Physics, Ministry of Education, School of Physics and Microelectronics, Zhengzhou University, Zhengzhou 450001, China
* Correspondence: guofm@zzu.edu.cn

Abstract: Nb_2CT_x is an important member of MXene family. It has attracted widespread attention because of its abundant functional groups, high hydrophilicity, high electrical conductivity as well as low ion transport barrier, showing great potential in various applications. In order to utilize the advantages of Nb_2CT_x MXene, the progress of preparation, properties and applications are reviewed in this work. This work focuses on different methods of Nb_2CT_x preparation and applications in electrochemical energy storage (supercapacitors and secondary batteries), electrocatalytic hydrogen evolution, photocatalytic hydrogen evolution, sensors, etc. Additionally, the main problems of self-stacking and prospect of Nb_2CT_x MXene are discussed.

Keywords: Nb_2CT_x; synthesis; application; energy conversion; electrochemical energy storage

check for updates

Citation: Guan, G.; Guo, F. A Review of Nb_2CT_x MXene: Synthesis, Properties and Applications. *Batteries* **2023**, *9*, 235. https://doi.org/10.3390/batteries9040235

Academic Editors: Sylvain Franger and Pascal Venet

Received: 11 January 2023
Revised: 31 March 2023
Accepted: 13 April 2023
Published: 19 April 2023

1. Introduction

MXene, a 2D layer-structured material, has high conductivity, excellent mechanical property and large surface area [1,2]. MXene consists of transition metal nitrides, carbides or carbonitrides. Its molecular formula is $M_{n+1}X_nT_x$, where M is the transition metals, including Ti, Sc, Cr, V, Zr, Nb, and Mo, X is carbon or nitrogen and T_x stands for surface terminals, including -F, -OH as well as -O groups [3,4]. Usually, MXene can be obtained by selectively etching the A atom (Si or Al atom) layers of MAX phase (precursor of MXene, M represents transition metal element; A represents main group element; X represents carbon or nitrogen.) [5,6]. Because of its chemical composition and unique structure, MXene and its composites have been applicated in electrochemical energy storage (supercapacitors and secondary batteries) [7], catalysis [8], sensors [9], electromagnetic interference shielding [10], etc.

So far, most of the research on MXene has focused on $Ti_3C_2T_x$, for the preparation of $Ti_3C_2T_x$ is quite mature. In MXene materials, as the number of atomic layers increases, the molecular mass increases and the theoretical capacity decreases. Therefore, compared with $Ti_3C_2T_x$, MXene with M_2X structure has a higher specific capacity. Nb_2CT_x exhibits outstanding conductivity, near zero bandgap, and has special metallic properties because of the flexible combination of surface functional groups [11,12]. Nb_2CT_x can be obtained by acid etching of the Nb_2AlC MAX phase. Theoretical studies have shown that Nb_2CT_x and its modified materials will show excellent performance in many fields because of the improved properties.

Figure 1 shows that Nb_2CT_x with different properties have been applied in various fields in recent years. Cheng et al. [13] have studied the charge storage mechanism of Nb_2CT_x in lithium-ion batteries, by combining density functional theory (DFT) calculations and complementary experiments. It is found that the outstanding electrochemical performance of Nb_2CT_x is mainly related to the unique structure of -O functional groups on Nb_2CT_x surface. As the oxidation states of O and Nb changes, Nb_2CT_x will store charge, while Li-ion can intercalate or deintercalation between the interlayers of Nb_2CT_x for charge compensation. The theoretical capacity value of Nb_2CT_x can reach 542 mAh/g [14]. Xin et al. [15] have shown that Nb_2CT_x nanosheet is an outstanding material as supercapacitor electrode by evaluating the theoretical quantum capacitances. It can be calculated

using the equation, $C_Q = e^2D(-Ve)$, where $D(E)$ is the electronic densities of state (DOS), E is the energy with respect to the Fermi level, V is the voltage of the electrode, and e is the elementary charge. The theoretical quantum capacitances of Nb_2CT_x electrode are 1091.1 and 1828.4 F/g at negative and positive electrodes, respectively. Nb_2CT_x is an excellent candidate for catalysis. In photocatalytic application, the structure of 2D Nb_2CT_x can promote photogenerated carrier to transfer from interior to Nb_2CT_x surface. This leads to improved separation efficiency and photodegradation performance [16]. Similarly, Nb_2CT_x has also been applied in electrocatalytic hydrogen evolution (HER) due to its abundant hydrophilic functional groups, especially the terminated O atoms. The Gibbs free energy ($\Delta G^a_{H^*}$) for the adsorption of atomic hydrogen is close to the ideal value (0 eV) [17]. In addition, Nb_2CT_x has also been applied in sensors due to its highly hydrophilic surface and high charge-carrier mobility [18].

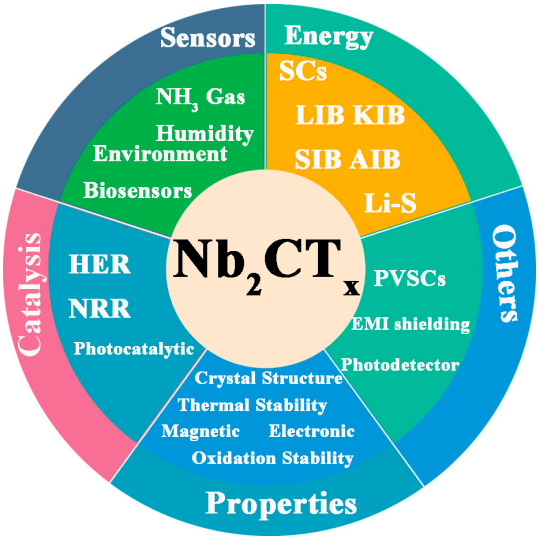

Figure 1. Different properties and applications of Nb_2CT_x.

The outstanding properties of Nb_2CT_x have ensured its applications in different areas, such as energy storage devices [19–22], electrocatalysis [23,24], photocatalysts [25,26], and sensors [27–29]. In addition, applications of Nb_2CT_x on other areas have also been reported, such as on perovskite solar cells (PVSCs) [30], photodetector [31], biomedicine [32], electromagnetic shielding [33], adsorbents [34], etc. In this paper, the progress of Nb_2CT_x preparation, its properties and different applications are reviewed, while also focusing on the exfoliating methods as well as applications in energy storage (supercapacitors and secondary batteries), photocatalytic hydrogen evolution, electrocatalytic hydrogen evolution, sensors, etc. Additionally, the main problems of self-stacking of Nb_2CT_x are discussed and prospects for the future are explored.

2. Synthesis

In Nb_2AlC MAX, the Nb-C bonds are strong, while the metal bonds of Nb-Al are relatively weak, therefore, Nb_2CT_x is usually obtained by selectively removing Al atom layers of Nb_2AlC. Even though the metal bond energy between the Nb-Al atomic layers is relatively weak, the bonding strength is still greater than that of the Van der Waals force. Hence, it seems difficult to peel the precursor into few-layer or monolayer using ultrasound-assisted liquid-phase exfoliation or other mechanical stripping method. Chemical exfoliation method is the most effective and widely used approach, where Nb_2CT_x can be prepared by etching away the Al atomic layer without destroying the Nb-C atomic layers. Figure 2 shows the structures of various types of MAX phases and their corresponding MXene structures obtained using chemical exfoliation method.

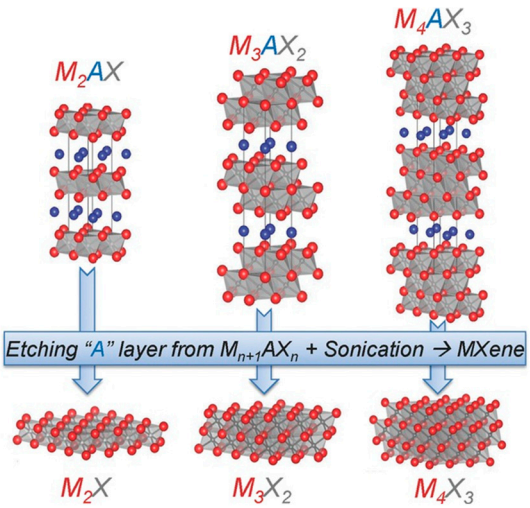

Figure 2. Structures of MAX phases and their corresponding MXene. Reprinted with permission. Copyright John Wiley & Sons, Inc., 2013 [35].

Studies have also shown that Nb_2CT_x can be intercalated by a variety of metal cations [36] or organic molecules [20] to increase the interlayer spacing, and to facilitate the etching of Al atoms and exfoliation of Nb_2CT_x nanosheets. After exfoliation, the single-layer or few-layer Nb_2CT_x nanosheets can be obtained.

2.1. Synthesis of Nb_2AlC

Most of Nb_2CT_x is obtained from Nb_2AlC MAX. The quality of Nb_2AlC MAX affects the quality of Nb_2CT_x nanosheets directly. In order to get Nb_2CT_x nanosheets with high quality, Nb_2AlC MAX with high quality should be prepared first. Many methods are developed to prepare Nb_2AlC MAX, such as high-temperature solid-state reaction method [37–40], self-propagating high-temperature synthesis (SHS) process [41–44] and spark plasma sintering technique (SPS) [45].

Stumpf et al. [38] have synthesized Nb_2AlC powders using the high-temperature solid-state reaction method. Firstly, high-purity Nb, NbC and Al powders are uniaxially compacted at 250 MPa to obtain powder particles, then Nb_2AlC powder is obtained by grounding particles at a high temperature of 1600 °C. Yeh et al. [41] have synthesized Nb_2AlC using a productive self-propagating SHS process. To obtain Nb_2AlC, Al_4C_3, Nb_2O_5 and Al undergo chemical reactions under different stoichiometric parameters and high temperatures (1200–1800 °C). Although these methods can prepare high-purity Nb_2AlC, the equipment and high temperature required for the synthesis lead to huge investment and production costs.

SPS is considered as an effective method for the synthesis of many ceramics. Compared with the thermocompression method, SPS shows obvious advantage in heating as it can be heated by pulsed direct current, and requires lower temperature and shorter cycle time. Zhou et al. [45] have synthesized Nb_2AlC using spark SPS, whereinhigh-purity Nb, Al and NbC powders are uniaxially compacted at 20 MPa and then vacuum sintered in a spark plasma at a heating temperature of 1450 °C.

Among all these preparation methods mentioned above, the preparation of Nb_2AlC using the SPS method has advantages in temperature, reaction time and cost, thus promises to be an efficient and commonly used method for the synthesis of Nb_2AlC.

2.2. Synthesis of Nb_2CT_x

Nb_2CT_x is usually obtained from Nb_2AlC MAX using the chemical exfoliation methods. Commonly used chemical etching methods include hydrofluoric acid (HF) etching [46–50], hydrofluoric acid/lithium fluoride (HCl/LiF) in situ generation of hydrofluoric acid etching [51,52], hydrothermal etching [53], Lewis acid molten salt etching [54,55] and electro-

chemical etching [56]. Etching with a high-concentration HF solution is currently the most common method for preparing Nb_2CT_x. Using the HF etching method, Zhao et al. [46] have obtained few-layer Nb_2CT_x nanosheets by changing the reaction temperature, time and other parameters, shown in Figure 3a. After HF etching, the densely packed layers of Nb_2AlC become unconsolidated, and the angle of (002) diffraction peak is smaller due to action of different surface functional groups and interlayer water molecules. In the meantime, Nb_2CT_x, exposed to the solution will combine with different functional groups (-OH, -F and -O). However, some Nb_2AlC usually remains in the Nb_2AlC prepared using the etching method. In Table 1, different experimental parameters of HF etching method is compared, since etching conditions will affect the purity and layer spacing of Nb_2CT_x [14,46,57–61]. As shown in Table 1, proper acid concentration, reaction temperature and reaction time will promote the etching reaction and benefit in obtaining pure Nb_2CT_x nanosheets.

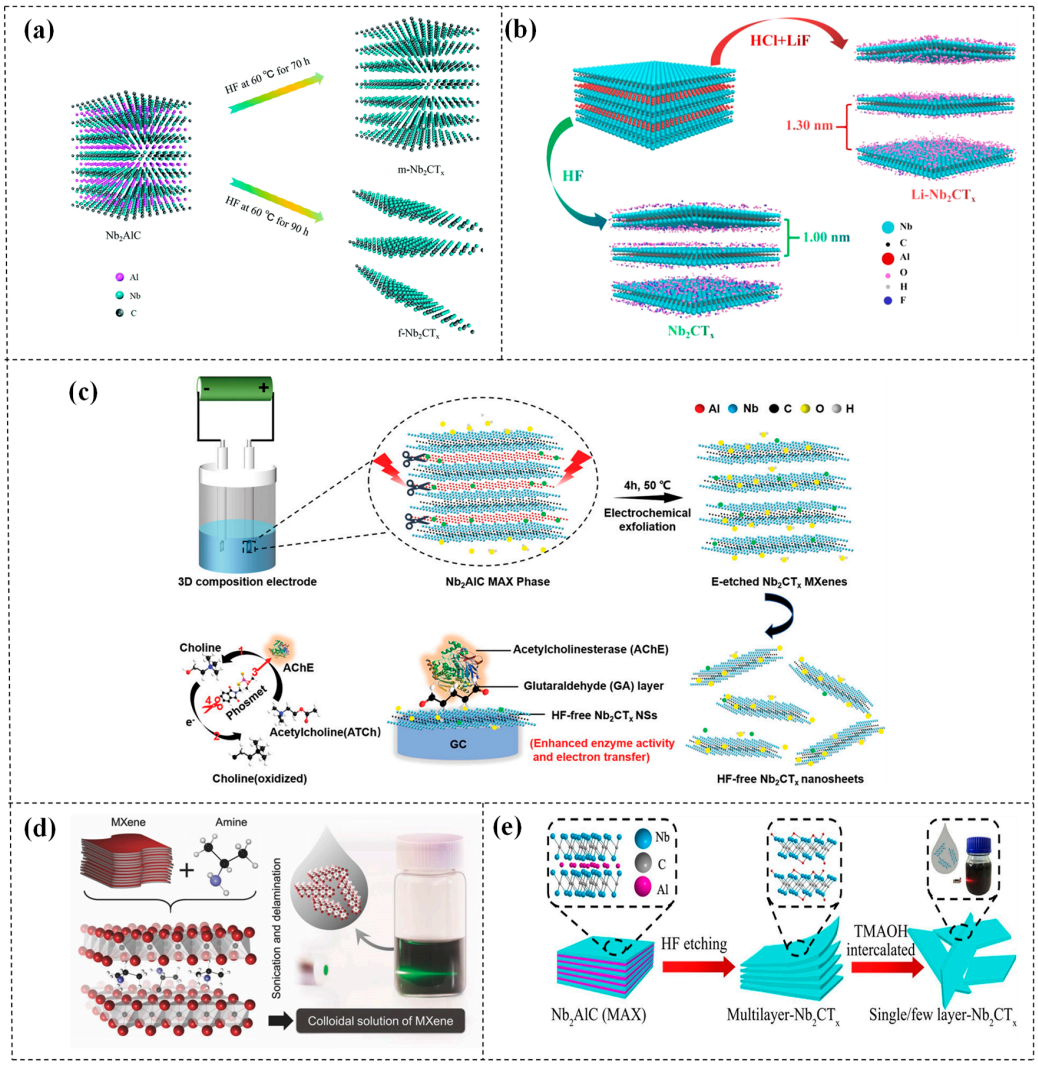

Figure 3. Synthesis and delamination of Nb_2CT_x. (**a**) Synthesis of Nb_2CT_x using HF etching method. Reprinted with permission. Copyright Royal Society of Chemistry, 2019 [46]. (**b**) Synthesis of Nb_2CT_x using HCl/LiF in situ generation of hydrofluoric acid etching method. Reprinted with permission. Copyright Elsevier, 2021 [51]. (**c**) Synthesis of Nb_2CT_x using electrochemical etching method. Reprinted with permission. Copyright John Wiley & Sons, Inc., 2020 [56]. (**d**) Delamination of Nb_2CT_x using isopropylamine (i-PrA). Reprinted with permission. Copyright John Wiley & Sons, Inc., 2015 [20]. (**e**) Delamination of Nb_2CT_x by intercalation with tetramethylammonium hydroxide (TMAOH). Reprinted with permission. Copyright Elsevier, 2020 [16].

Table 1. Different parameters of HF etching method for the preparation of Nb_2CT_x.

Etching Solution	Temperature/°C	Time/h	References
50% HF	25	240	[14]
40% HF	60	90	[46]
48% HF	55	48	[57]
50% HF	55	72	[58]
48% HF	80	24	[59]
50% HF	30	24	[60]
40% HF	50	72	[61]

Since the high concentration of hydrofluoric acid is harmful to humans and the environment, developing environmentally friendly and milder methods to prepare Nb_2CT_x is urgent and important. Hydrofluoric acid/lithium fluoride (HCl/LiF) in situ generation of hydrofluoric acid etching method is an effective alternative to the HF etching method. As Figure 3b shows, Xiao et al. [51] have obtained few-layer Nb_2CT_x using HCl/LiF in situ generation of hydrofluoric acid etching method, where Li^+ can be embedded in the Nb_2CT_x layers to facilitate the delamination of Nb_2CT_xnanosheets. However, HF is still generated and released during the HCl/LiF in situ generation of hydrofluoric acid etching process, and thus this method is harmful to humans and environment in some ways. Therefore, it is imperative to propose green preparation methods which can avoid the direct use and release of hydrofluoric acid. Peng et al. [53] have obtained Nb_2CT_x using solvothermal treatment by mixing hydrochloric acid (HCl) and sodium tetrafluoroborate ($NaBF_4$) together, followed by ultrasonication and intercalation. Specifically, the mixture of $NaBF_4$, HCl and Nb_2AlC is hydrothermally reacted at 180 °C for 15–35 h. The etching process takes place in a confined hydrothermal system, without exposure to toxic hydrofluoric acid vapors. The hydrothermal method can remove the Al layer more completely compared to traditional HF etching method.

Since -F functional groups are electronegative, too much -F functional groups will greatly reduce the conductivity of MXene [36], so proposing fluorine-free etching methods is also necessary. In recent years, some fluorine-free etching methods have been reported, such as to obtain Ti_2CT_x using electrochemical etching method [62] and to obtain $Ti_3C_2T_x$ by etching Ti_3AlC_2 using the molten salt method [63]. Similar to these methods of obtaining $Ti_3C_2T_x$ and Ti_2CT_x, fluorine-free methods to obtain Nb_2CT_x have also been reported in recent years.

Song et al. [56] have synthesized fluoride-free Nb_2CT_x flakes using an electrochemical etching method (E-etching method), as shown in Figure 3c. This method is carried out in a three-electrode system where Nb_2AlC phase powder and carbon black are mixed and evenly drop-cast onto the CFC substrate. This electrode is oxidized in HCl electrolyte for 4 h at 50 °C with a voltage of 1 V to etch away the Al atomic layers. Li et al. [55] have used a fluoride-free method using direct redox coupling of the cation from the Lewis acid molten salt and the Al atom of Nb_2AlC. Specifically, AgCl is used as salt, while Nb_2AlC is mixed with AgCl, KCl and NaCl in a molar ratio of 1:5:2:2, and reacted at 700 °C for about 24 h. During this reaction, Al atoms will be oxidized by AgCl and eventually removed from Nb_2AlC to obtain Nb_2CT_x.

In general, hydrofluoric acid etching is the most commonly used method for synthesizing Nb_2CT_x. However, considering the danger of hydrofluoric acid to humans and the fact that fluorine functional groups will reduce the electrochemical performance of Nb_2CT_x, many fluorine-free etching methods have been suggested. However, these methods still have problems, such as harsh reaction conditions or low yields. Therefore, it is still important to explore more efficient fluorine-free etching methods.

2.3. Delamination of Nb_2CT_x

After the Nb_2AlC etching reaction, the Al atoms are selectively removed, and replaced with functional groups, such as -F, -OH as well as -O. The obtained Nb_2CT_x layers are held together by hydrogen bonds and weak Van der Waals forces. However, the Nb_2CT_x sheets are multi-layered, and further delamination/exfoliation processing is required to form single-layer/few-layer Nb_2CT_x sheets. The specific surface area of two-dimensional materials will be greatly increased after further delamination.

Generally, the materials for delamination involve organic, ionic molecules or inorganic cation. Non-alkaline organic solvent intercalation is an effective way to obtain few-layer Nb_2CT_x. Such organic solvent intercalants include DMSO [26,64], isopropylamine (i-PrA) [20,48], etc. For example, Mashtalir et al. [20] have obtained few-layer Nb_2CT_x sheets using isopropylamine (i-PrA), as shown in Figure 3d. When mixed with water, i-PrA can form ammonium cation R-NH_3^+, which can be intercalated between Nb_2CT_x layers using electrostatic force. In addition, the i-PrA molecule has a three-carbon-atom alkyl tail, which can overcome the intercalation steric hindrance and push the Nb_2CT_x nanosheets apart, resulting in weaker interlayer interactions and leading to the delamination of Nb_2CT_x.

Cation intercalation, treating Nb_2CT_x with alkalization, is another widely used method. The intercalants include LiOH [14], KOH [36], TMAOH [16,65], and TPAOH [28,66,67]. As shown in Figure 3e, Cui et al. [16] have obtained few-layer Nb_2CT_x sheets by intercalating with tetramethylammonium hydroxide (TMAOH) for about 3 days at room temperature. Thus, the numerous functional groups on the surface of Nb_2CT_x nanosheet make it negatively charged. In order to achieve charge balance, H^+ will enter the interlayers. When treated with alkali, the cations of the alkali will replace H^+ and insert between the layers. After cation intercalation, the layer spacing of Nb_2CT_x will be larger and the -F functional groups will be replaced by hydroxyl functional groups. The intercalated alkali cations will weaken the interaction between the Nb_2CT_x sheets, so single-layer/few-layer Nb_2CT_x flakes can be obtained after simple exfoliation, such as shaking or water-bath sonication.

3. Structure and Properties of Nb_2CT_x

3.1. Structure of Nb_2CT_x

The Scanning Electron Microscope (SEM) image (Figure 4a) and Transmission Electron Microscope (TEM) image (Figure 4b) show that the few-layer Nb_2CT_x sheets are ultrathin and transparent. The high-resolution transmission electron microscopy (HRTEM) image (Figure 4c) and the selected area electron diffraction (SAED) pattern image (inset of Figure 4c) of the Nb_2CT_x nanosheets show good crystallinity. A clear crystal lattice patten of (0001) crystal plane can be seen, showing good single crystal characteristics [46]. The X-ray diffraction (XRD) image (Figure 4d) indicates that the (002) peak of few-layer Nb_2CT_x sheets shifts toward a lower angle, suggesting a larger interspacing due to the elimination of Al atoms [57].

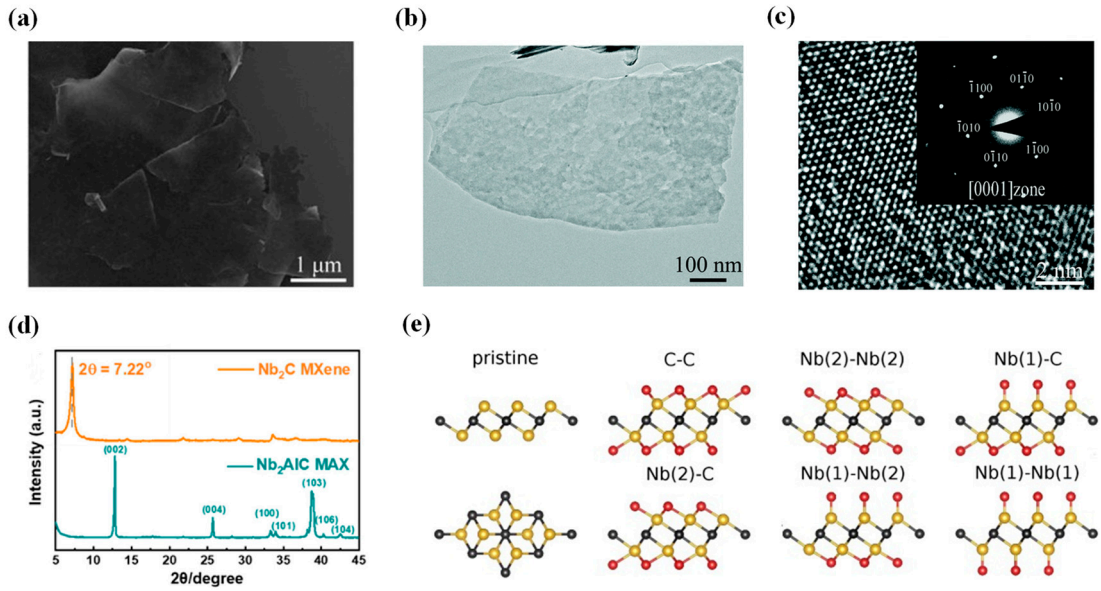

Figure 4. Characterization and structure of Nb_2CT_x. (**a**) SEM image of Nb_2CT_x, (**b**) TEM image of Nb_2CT_x, (**c**) HRTEM image of Nb_2CT_x. Reprinted with permission. Copyright Royal Society of Chemistry, 2019 [46]. (**d**) XRD image of Nb_2CT_x. Reprinted with permission. Copyright American Chemical Society, 2022 [57]. (**e**) Structure of Nb_2C and Nb_2CX_2 [68]. Copyright John Wiley & Sons, Inc., 2015.

The crystal structure of computationally modeled Nb_2C MXene is similar to that of 1T-MoS_2, including three layers with Nb-C-Nb sequence in a 3 × 3 × 1 supercell. The C layer is sandwiched by two Nb layers; C layers and Nb layers are stacked along the hexagonal c-axis [57]. Because of the highly unsaturated surface in Nb_2C, functionalized elements (F, O, OH and N) can be easily trapped in the hollow sites. Figure 4e [68] exhibits the modeling structures, including Nb_2C and Nb_2CX_2, where X groups can be located at top of a Nb (1) atom (top layer), a C atom and a Nb (2) atom (bottom layer), and both Nb_2C sides, therefore, there are a total of six configurations of adsorption sites.

3.2. Properties of Nb_2CT_x

Seredych et al. [69] have explored the thermal stability of Nb_2CT_x using mass spectrometry analyses and combined thermogravimetric. Nb_2CT_x etched by HF tends to release water at 246 °C and the main phase transition occurs at 807 °C, with a weight loss of 10–15 wt%. The weight loss coincides with the massive release of CO_2 as well as CO, indicating a possible transformation of Nb_2CT_x into the stable corresponding massive carbides. The Nb_2CT_x, further delaminated by TMAOH, has a weight loss of about 8.5 wt%, in a temperature range of 50 °C to 600 °C. NH_3, NH_2, and NH_4^+ species release because of the decomposition process and desorption process of TMA^+ ions. The results indicate that the intercalant is strongly bound to the surface of Nb_2CT_x nanosheets to hinder water adsorption. The transformation temperature slightly increases to 820 °C with less mass loss of about 4 wt%, indicating a higher stability of Nb_2CT_x. Therefore, intercalants, such as TMAOH, can replace water and affect the decomposition products at low-temperature, making Nb_2CT_x with better thermal stability.

Babar et al. [70] have explored the magnetic properties of Nb_2CT_x. The peculiar magnetic properties of Nb_2CT_x shows the existence of Meissner effect, and Nb_2CT_x is supposed to have superconductivity (SC) with the transition temperature of 12.5 K. Evaluated with the DFT first-principles calculation, the Nb_2CT_x shows a negative magnetic moment, which corresponds well to the experimental diamagnetic nature. Both the experimental analysis and calculation indicate Nb_2CT_x showing a superconductor-like diamagnetic behavior. The superconductivity-like magnetic property in Nb_2CT_x can be attributed to the higher density-of-states at the Fermi level and strong electron–phonon interaction [71].

Xu et al. [72] have studied the electronic properties and structural stability of Nb_2CT_x based on DFT calculations, paying special attention to the influence of surface groups. The study suggests that Te and O groups are more inclined to locate at the central C hollow sites on both Nb_2CT_x sides. The interaction strength between different functional groups and Nb atoms will gradually decrease from O to S, Se and to Te. This study has further analyzed bonding interactions using projected crystal orbital Hamiltonian populations. As the surface terminal gains less electrons from O to Te group, the integrated projected crystal orbital Hamilton population (pCOHP) value decreases gradually from O to Te. The altered interactions can also affect the electronic performance of Nb_2CT_x. This study has found that it is the different types of surface groups that determine the electronic properties and conductivity of Nb_2CT_x, with adsorption sites as a secondary factor. That is, Nb_2CO_2 and Nb_2CTe_2 are metallic, while Nb_2CS_2 and Nb_2CSe_2 can be metallic or semiconducting, depending on the adsorption sites of different surface groups on Nb_2CT_x.

Halim et al. [73] have obtained Nb_2CT_z and Ti_2CT_z film via physical vapor deposition on sapphire and LiF/HCl etching method, and then measured the optical and electronic properties of these films. Ti_2CT_z film exhibits metallic behavior while Nb_2CT_z film is not metallic, which can be supported by optical properties via spectroscopic ellipsometry measurements. The difference in optical response between Nb_2CT_z film and Ti_2CT_z film can be attributed to the absorption of Nb_2CT_z film near infrared. Additionally, the resistivity of Nb_2CT_z film increases when temperature decrease, because of the percolation between Nb_2CT_z flakes. The different optical and electronic properties of these films are influenced by the type of transition metal.

Palisaitis et al. [74] have investigated the stability of Nb_2CT_x in plan-view geometry using electron energy loss spectroscopy (EELS), atomically resolved scanning transmission electron microscopy (STEM) as well as STEM simulations. This research has found that the Nb adatoms on Nb_2CT_x surface can attract and be linked to ambient O and then form clusters which will ripen over time, leading to the destruction of Nb_2CT_x structure stability. Considering the structure stability at a long time, the adatoms on the Nb_2CT_x surfaces are detrimental for Nb_2CT_x structure. Echols et al. [75] have explored ways to enhance the oxidation stability of Nb_2CT_x. It is found that the shelf life of Nb_2CT_x can be significantly improved with low temperature storage, using antioxidants, increasing the concentration of Nb_2CT_x solution, etc.

4. Applications

4.1. Secondary Batteries

MXene has rich chemical and structural diversity, and is a promising material for secondary batteries electrode. When the layer of MXene materials increases, the molecular mass increases, so the theoretical capacity will decrease [76]. Hence, compared to M_3X_2 and M_4X_3, the M_2X structured MXene tends to have a higher specific capacity [77]. Nb_2CT_x MXene, showing low diffusion barriers, fast ion mobility and low average intercalation potentials, has generated great interests in recent years. Currently, the research on Nb_2CT_x application on secondary batteries is still at the exploratory stage. Taking lithium-ion batteries as an example, Nb_2CT_x has a low lithium-ion diffusion barrier (<0.1 eV), and thus Li^+ ions can easily intercalate into the Nb_2CT_x nanosheets. The surface functional groups of Nb_2CT_x also affect the lithium storage performance of Nb_2CT_x. The specific capacity of Nb_2CT_x with -O functional groups are higher than that of Nb_2CT_x with -F and -OH functional groups. The -F and -OH functional groups can inhibit the adsorption of lithium ions, which is detrimental to the electrochemical properties. The reaction of Nb_2CT_x with -O functional groups to adsorb lithium ions is as follows:

$$Nb_2CT_xO_2 + 2Li \leftrightarrow Nb_2CT_xO_2Li_2 \quad (1)$$

4.1.1. Lithium Ion Battery

As an important type of energy storage device, Lithium-ion batteries (LIBs) are playing an increasingly important role in our society owing to their ability to offer power for both our daily life and industrial manufacturing [78–80]. Numerous studies on Li-ion battery materials have been reported in recent years. For example, the first DFT calculations of a high-energy, 5 Volt rechargeable Li-ion battery cathode material $Li_2CoMn_3O_8$ were performed by Eglitis and Borstel [81]. It was found that the reversible capacity of Nb_2CT_x is higher than that of $Ti_3C_2T_x$, and the capacity value of Nb_2CT_x can reach 542 mAh/g [14], which is much larger than that of $Ti_3C_2T_x$ (320 mAh/g). However, considering the strong Van der Waals force between Nb_2CT_x layers, Nb_2CT_x nanosheets are easy to aggregate or stack together. The self-restacking will lead to densely packed structure, reducing the specific surface area and increasing difficulty in the transportation of ions, thus to decreasing the rate performance and cycling performance of Nb_2CT_x electrodes. Qi et al. [77] have reported that the specific capacity of Nb_2CT_x after 200 cycles at 500mA is less than 200 mAh/g, which is far from the theoretical value. Therefore, strategies should be carried out to improve the electrochemical properties from Nb_2CT_x.

Reports have been published to solve the above problems in order to fully utilize the electrochemical properties of Nb_2CT_x [82–86] Li et al. [82] have mixed Nb_2CT_x with 1,3,5-benzenetricarboxylic acid (BA) to obtain BA-Nb_2C, as shown in Figure 5a. BA molecules can be anchored into Nb_2CT_x nanosheets through hydrogen bonding interaction between Nb_2CT_x sheets and BA molecules, enlarging the interlayer spacing and enhancing the stability of Nb_2CT_x. Figure 5b shows that BA-Nb_2C exhibits a larger specific surface area which can facilitate the Li^+ diffusion, provide more active sites, and improve the capability

rate of Nb_2CT_x. The BA-Nb_2C electrode exhibits a high specific capacitance of 328.2 mAh/g at 0.1A/g, as shown in Figure 5c.

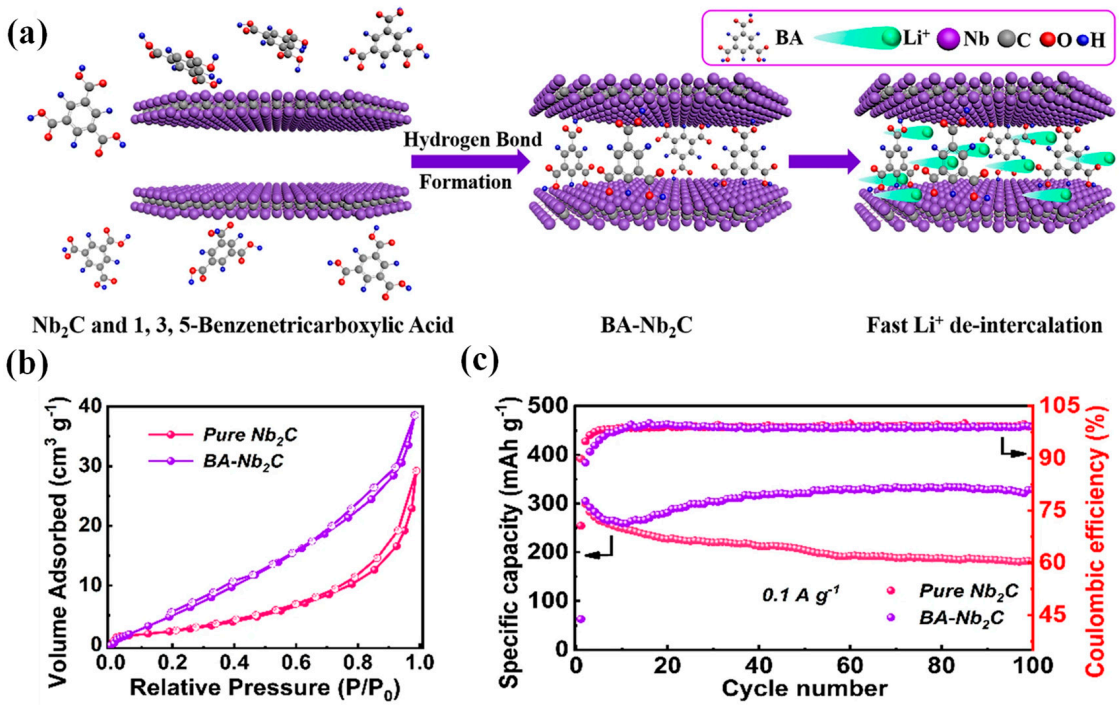

Figure 5. BA-Nb_2C as anode materials for LIBs. (**a**) Schematic illustration of the synthesis mechanism, (**b**) Nitrogen adsorption–desorption isotherms of pure Nb_2C and BA-Nb_2C, (**c**) cycling stability of BA-Nb_2C at 0.1 A/g. Copyright Springer Nature, 2022 [82].

The surface functional group of MXene plays an important role in the electrochemical reaction [84,85]. The -F functional and hydroxyl groups on Nb_2CT_x surface can hinder the diffusion of Li-ions in the interlayer, thereby greatly reduce the lithium storage specific capacity [86]. However, the -O groups on Nb_2CT_x surface will promote the diffusion and adsorption of Li-ions and effectively inhibit the formation of lithium dendrites [13]. Zhao et al. [14] have mixed LiOH with Nb_2CT_x to introduce more oxygen-containing functional groups and analyzed the corresponding electrochemical properties and Li storage dynamics. The surface functional groups (-O, -OH and -F) of Nb_2CT_x nanosheets changes when annealed at different temperatures. After annealing at 400 °C, -O surface functional groups of Li^+ intercalated Nb_2CT_x increase while the -OH and -F groups decrease. The Li-Nb_2CT_x-400 electrode shows a high specific capacity of 448 mAh/g at 0.05 A/g owing to the large number of -O surface functional groups.

4.1.2. Sodium Ion Battery

Sodium ion batteries (SIBs) have become a promising alternative to LIBs because of certain advantages, such as low cost, abundant sodium resources and similar energy storage mechanism. However, the radius of Na-ion is larger than that of Li-ion, and the development of SIBs is constrained by the short of suitable anode materials [87,88]. MXene, with its unique properties and structure, is promising to serve as a new type of anode material for SIBs [89,90]. As shown in Figure 6a, Yuan et al. [77] have constructed a robust 3D Nb_2CT_x@MoS_2@C composites, by hydrothermal synthesis of MoS_2 and carbon coating on Nb_2CT_x framework. The Nb_2CT_x@MoS_2@C composites show a reinforced cross-linked three-dimensional structure (Figure 6b). The high specific surface area and stable structure can better utilize the electrode material. The Nb_2CT_x@MoS_2@C electrode shows an improved charge transfer efficiency, and avoid structural collapse or volume expansion caused by Na-ion intercalation. The Nb_2CT_x@MoS_2@C exhibit a high capacity of 530 mAh/g after

200 cycles test in 0.1 A/g (Figure 6c). Zhang et al. [91] have prepared a sandwich-like composite including N-doped carbon nanotubes (N-CNTs) and Nb_2CT_x nanosheets using the electrostatic self-assembly approach. The N-CNTs are trapped between two MXene layers as conductive agents and spacers. In addition, the N-doped sites on the carbon nanotube walls can act as defects, promoting the diffusion and storage of Na-ion. The N-CNT@Nb_2C is supposed to have good electrochemical performance as Na-ion batteries anode. Xiao et al. [92] have synthesized Ag-Nb_2CT_x composite by physically mixing Ag nanoparticles and Nb_2CT_x nanosheets. The Ag-Nb_2CT_x can provide larger specific surface area and higher conductivity. The Ag-Nb_2CT_x shows a capacity of 183 mAh/g at 0.05 A/g after 50 cycles in Na-ion battery.

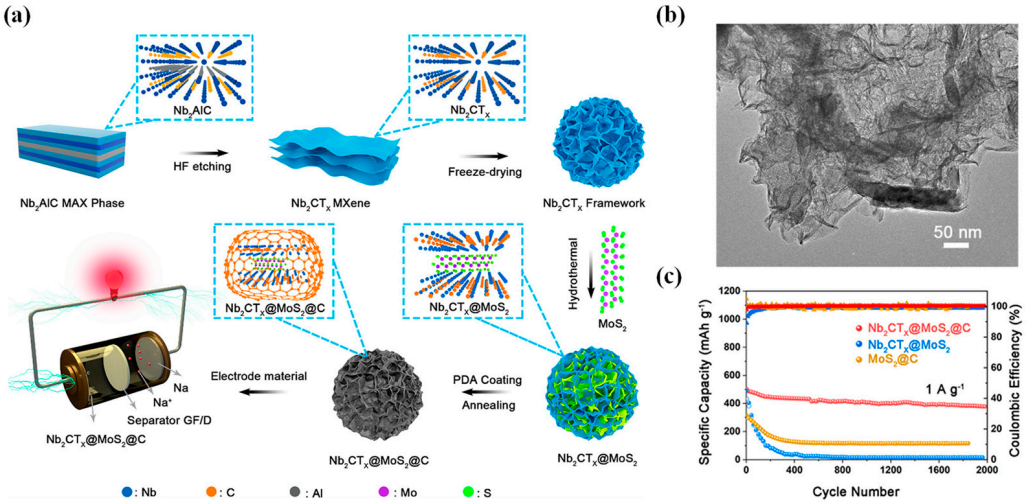

Figure 6. Applications of Nb_2CT_x in SIBs. (**a**) Schematic illustration of preparation of the Nb_2CT_x@MoS_2@C hybrid, (**b**) TEM image of Nb_2CT_x@MoS_2@C, (**c**) Cycling stability of Nb_2CT_x@MoS_2@C at 1 A/g. Copyright American Chemical Society, 2021 [77].

4.1.3. Potassium Ion Battery

Potassium-ion batteries (KIBs) is also a potential alternative to LIBs because of the low cost and abundance of potassium-related resources. However, the ion migration of electrodes is difficult because of the much larger radius of K-ion compared to Li-ion [93,94]. Therefore, developing suitable electrode materials for KIBs is essential. The unique structure and excellent conductivity of Nb_2CT_x make it an ideal electrode candidate for KIBs [95]. As shown in Figure 7a, Liu et al. [58] have prepared in situ carbon-intercalated and surface-modified Nb_2CT_x as electrode for Potassium-ion batteries. The carbon-intercalated Nb_2C nanocomposite (Nb_2C/C) can be obtained by intercalating dodecylamine (DDA) into the Nb_2CT_x layers, followed by annealing (Figure 7b). The Nb_2C/C electrode shows less surface functional groups, enlarged interlayer spacing as well as increased specific surface area. The Nb_2C/C electrode, with high electrical conductivity and good K^+ diffusion coefficient, performs a specific capacity of 199.8 mAh/g at 0.02 A/g (Figure 7c). Mao et al. [20] have prepared self-standing composites of Nb_2CT_x and reduced graphene (rGO) (3D-rGO/Nb_2C) using the electrostatic self-assembly approach. The paper electrode with 3D porous network can provide more active sites and promote the transfer of K^+. The 3D-rGO/Nb_2C shows a good capacity of 139 mAh/g after 1000 cycles at 500 mA/g, owing to the diffusion and pseudocapacitive mechanism in potassium ion storage.

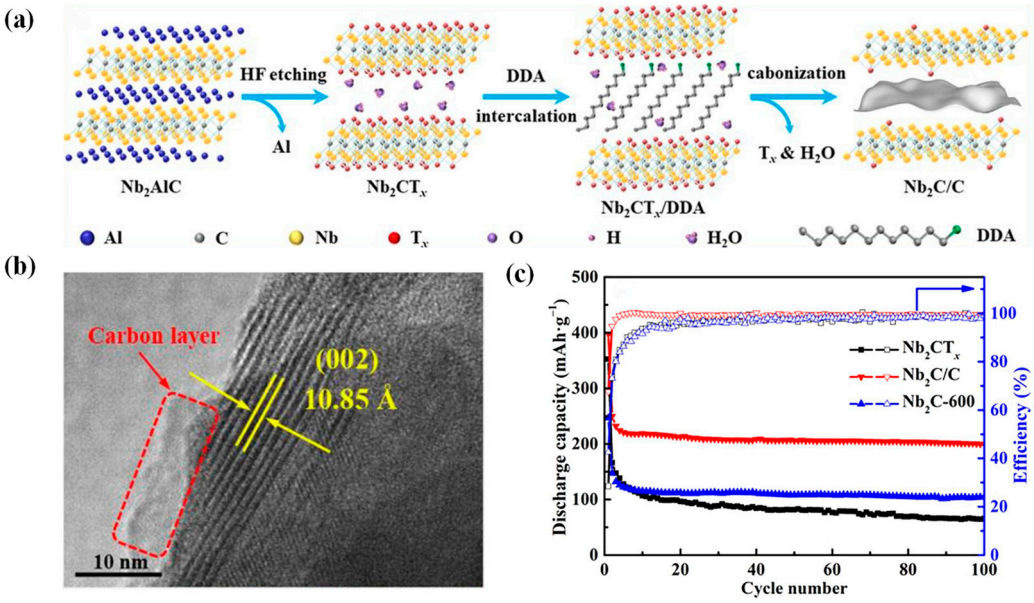

Figure 7. Applications of Nb_2CT_x in KIBs. (**a**) Schematic illustration for the synthesis of Nb_2C/C, (**b**) HRTEM image of Nb_2C/C, (**c**) Specific capacity of Nb_2C/C at 0.02 A/g. Copyright Elsevier, 2022 [58].

4.1.4. Lithium Sulfur Battery

Lithium-sulfur (Li-S) batteries have been considered as the best alternative to LIBs because of advantages such as long cycle life, low cost of active materials, as well as high energy density. However, the commercialization of this technology has been plagued by some key challenges, such as the insulating shuttling effect of sulfur cathodes, volume changes during charging/discharging, and poor electronic/ionic conductivity [96,97]. As previously reported, MXene with unique two-dimensional structure, negatively charged surface, and high conductivity can immobilize soluble polysulfides by adsorption to suppress the shuttling effect [98,99]. As shown in Figure 8a, Song et al. [100] have designed Nb_2C/Nb_2O_5 heterostructures using water vapor etching. The Nb_2C has high adsorption capacity, while Nb_2O_5 can catalyze the activity of lithium polysulfides. Meanwhile, the accordion-like and porous structure (Figure 8b,c) formed during water vapor etching can suppresses the aggregation of Nb_2C sheets and Nb_2O_5 nanoparticles, promote Li^+ transport and facilitate diffusion of the anchored lithium polysulfides. The S-Nb_2C/Nb_2O_5 electrode exhibits a capacity of 621 mAh/g after 500 cycles test at 1.0 C (Figure 8d). By freeze-drying, Zhong et al. [101] have prepared petal-like Nb_2CT_x and MoS_2 is grown on the surface of Nb_2CT_x via hydrothermal method. The Nb_2CT_x and MoS_2 is deemed to form a heterojunction owing to their high lattice adaptability. The MoS_2/Nb_2C heterojunction structure is favorable for the conductivity and adsorption capacity of lithium polysulfides. The specific capacity of MoS_2/Nb_2C cathode is 919.2 mAh/g at the current density of 0.2 C.

In addition to LIBs, SIBs, KIBs, and LSBs, Nb_2CT_x has also been applied to other batteries. The calcined Nb_2CT_x cathode used for aluminum batteries (Al batteries) shows a specific capacity of 08 mAh/g at 0.2 A/g after 500 cycle tests [57]. Li et al. [102] have proposed a new method of achieving high-energy-density MXene electrodes with a distinct discharge voltage plateau for aqueous zinc ion batteries. The authors use a high-voltage-scanning approach to trigger the behavior of Nb_2CT_x MXene cathode in aqueous Zn-ion batteries, which shows a stable Zn^{2+} storage with a 1.55 V plateau. The energy density of the MXene electrode reaches 146.7 Wh/kg, which is much higher than that of the capacitive Nb_2CT_x electrode and other conventional cathodes.

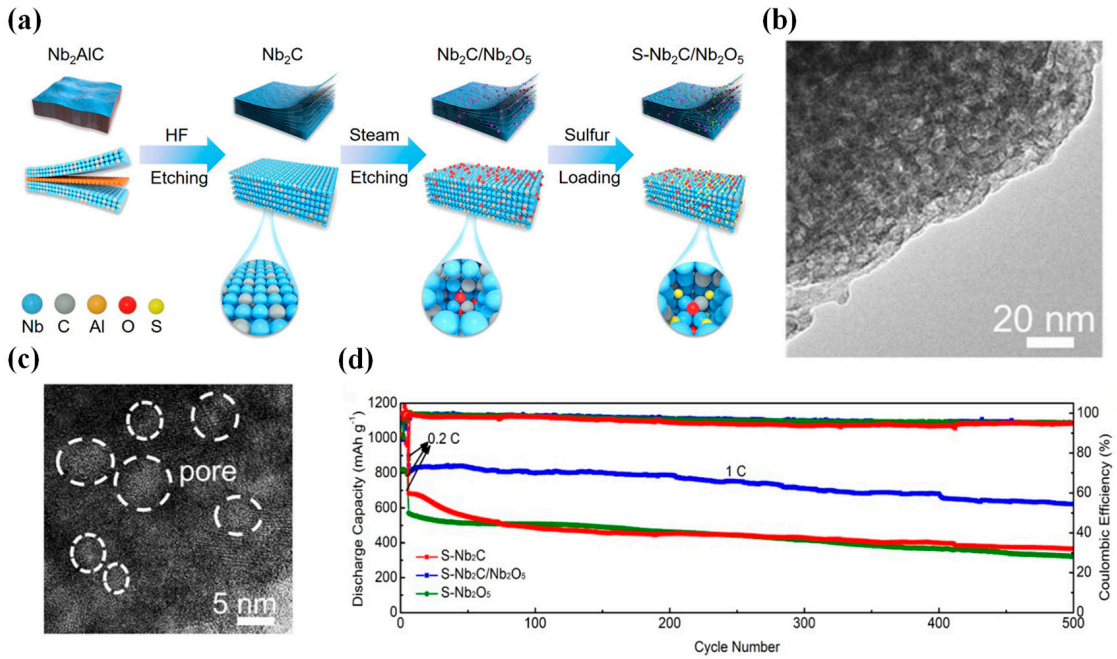

Figure 8. Applications of Nb_2CT_x in LSBs. (**a**) Schematics of preparation of S-Nb_2C/Nb_2O_5 heterostructures, (**b**,**c**) TEM images of Nb_2C/Nb_2O_5, (**d**) Cycling stability of S-Nb_2C/Nb_2O_5 electrodes at 1.0 C. Copyright Elsevier, 2022 [100].

Table 2 lists the performance of Nb_2CT_x with its derivative materials for secondary batteries by category.

Table 2. The specific capacities of Nb_2CT_x for secondary batteries.

Battery	Materials	Current Density	Cycles	Capacity (mAh/g)	References
LIB	Li-Nb_2CT_x-400	2 A/g	2000	342	[14]
LIB	Nb_2CT_x-CNT	2.5 C	300	430	[20]
LIB	Chl@Nb_2C	0.5 A/g	200	163	[77]
LIB	BA-Nb_2C	1 A/g	500	261.7	[82]
LIB	Nb_4N_5@Nb_2C	2 A/g	800	109.2	[83]
KIB	3D-rGO/Nb2C	0.5 A/g	1000	139	[21]
KIB	Nb_2C/ rGO	2 A/g	500	301.7	[94]
SIB	Nb_2CT_x@MoS_2@C	1 A/g	2000	403	[76]
SIB	Ag-Nb_2CT_x	0.05 A/g	50	183	[93]
Li-S	Nb_2C/Nb_2O_5	1.0 C	500	621	[100]
Li-S	MoS_2/Nb_2C	0.2 C	200	919.2	[101]
AIB	Nb_2CT_x	0.5 A/g	500	80	[57]

The restacking of Nb_2CT_x will impair the electrochemical properties, by hindering the transport of electrolyte ions inside the electrode and reducing the utilization of active sites in Nb_2CT_x electrode materials. the functional groups also greatly affect the electrochemical properties. In this section, different applications of Nb_2CT_x in secondary batteries have been introduced, to provide solutions or strategies in improving the electrochemical performance of Nb_2CT_x. Methods of intercalation in Nb_2CT_x nanosheets can effectively inhibit the restacking, with the intercalation materials of organic compounds [82,96], carbon materials [91], and metals [93]. Regulation the functional groups of Nb_2CT_x (for example, by substituting -O functional groups for -F, and -OH [14]), can obviously improve the ability of Nb_2CT_x to store charges. Studies have also shown that, increasing the ion transport channels of Nb_2CT_x by manufacturing porous or three-dimensional structures can also

effectively improve the electrochemical performance [20,76,100]. All these methods have obvious effects on the specific capacity, cycle life or rate performance of Nb_2CT_x.

4.2. Supercapacitors

Supercapacitors have been an important and widely applicated electrochemical energy storage device because of their high power density, fast charge–discharge capability and long-cycle stability [59,103]. For electrode materials of supercapacitors, the charge storage mechanism is an electrical double-layer capacitance mechanism and pseudo-capacitance mechanism [104,105]. In electric double-layer capacitive mechanism, ions store charges through electrostatic adsorption at the interface between supercapacitor electrodes and electrolytes, while in pseudocapacitive mechanism, ions store charges via fast reversible redox reactions on the surface of active materials. MXene with abundant surface functional groups, high electrical conductivity and rapid redox reactions on the surface is deemed to be an ideal pseudocapacitive material [106,107].

Nb_2CT_x is theoretically predicted to be an excellent electrode material with higher specific areal capacitance and gravimetric capacitance than $Ti_3C_2T_x$. Nb_2CT_x can provide redox-active Nb sites for pseudocapacitive-intercalation and the Nb element in Nb_2CT_x has a wider chemical valence or better electrochemical activity compared with that of Ti element [108]. However, the strong Van der Waals force between Nb_2CT_x sheets easily results in the aggregation of Nb_2CT_x nanosheets, leading to the degradation of electrochemical performance of Nb_2CT_x electrode. Recently, many works on Nb_2CT_x in supercapacitors have been devoted to improve the electrochemical performance. s. The electrochemical performance of Nb_2CT_x and its composites are listed in Table 3.

Table 3. The specific capacities of Nb_2CT_x for supercapacitors.

Materials	Electrolyte	Capacitance	References
Nb_2C/Ti_3C_2	1 M H_2SO_4	584 F/g at 2 A/g	[59]
Nb_2CT_x/CNT	1 M H_2SO_4	202 F/g at 2 mV/s	[109]
$Ti_3C_2T_x/Nb_2CT_x$	2 M H_2SO_4	370 F/g at 2 mV/s	[60]
Co_3O_4-Nb_2CT_x	6 M KOH	1016 F/g at 2 mV/s	[110]
Nb_2CT_x	1 M $LiSO_4$	154 F/g at 5 mV/s	[111]
S-P-NNO/f-Nb_2CT_x	1 M $LiPF_6$	157 mAh/g at 2.0 A/g	[112]

Nasrin et al. [59] have prepared Nb_2C/Ti_3C_2 (NCTC) heterointerface nanostructures via one-pot synergistic in situ etching of Nb_2C/Ti_3C_2. The NCTC is synchronized to enhance surface dynamics of charge storage by exposing more active sites and ion diffusion channels. With the individual and synergistic charge storage at the heterointerface, the NCTC shows a pseudocapacitive property with a specific capacitance of 584 F/g at 2 A/g. Xiao et al. [109] have mixed carbon nanotubes with Nb_2CT_x to enlarge the interlayers spacing of Nb_2CT_x sheets. The conductive CNT can improve the rate ability of Nb_2CT_x/CNT. The Nb_2CT_x /CNT//AC asymmetric supercapacitor, with Nb_2CT_x/CNT and activated carbon as electrodes, exhibits an areal capacitance of 462.0 mF/cm^2. Li et al. [60] have prepared flexible all-MXene hybrid films by mixing Nb_2CT_x and $Ti_3C_2T_x$ together. With the introduction of $Ti_3C_2T_x$ nanosheets, the interlayer spacing of Nb_2CT_x is increased and the stacking of MXene sheets is hindered. The flexible all-MXene film supercapacitor demonstrates a specific capacitance of 370 F/g at 2 mV/s and a good performance rate. As shown in Figure 9a, Shen et al. [110] have introduced Co_3O_4 into Nb_2CT_x layers using the electrostatic self-assembly approach to form a robust 2D cross-linked structure. Figure 9b shows that Co_3O_4 nanoparticles (marked in yellow circles) are uniformly distributed on Nb_2CT_x surface to suppress the self-restacking of Nb_2CT_x sheets and provide more active sites. The 2D cross-linked Co-MXene electrode shows a specific capacitance of 730 F/g at 20 mV/s (Figure 9c). Li et al. [22] have constructed Nb_2CT_x hydrogels via a 4D printing using a heat-stimulated self-assembly process, with the conducting polymer PEDOT:PSS working as the crosslinker. The 3D porous structured Nb_2CT_x hydrogels, shows with

enhanced mechanical strengths, high specific surface area, good electrical conductivities and good electrochemical performance.

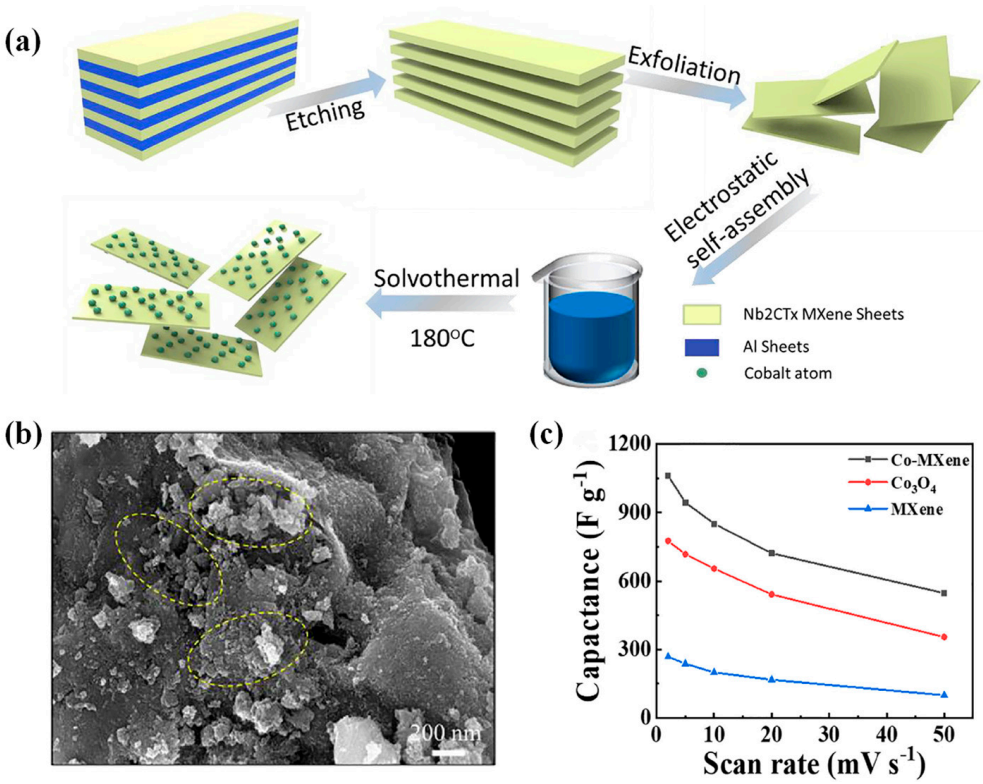

Figure 9. Applications of Nb_2CT_x in supercapacitors. (**a**) Schematic illustration of the preparation procedure of Co-MXene, (**b**) SEM images of the Co-MXene composites, (**c**) Specific capacitance of Co-MXene at different current densities. Copyright Elsevier, 2022 [110].

Liao et al. [111] have studied the capacitance behavior of Nb_2CT_x under cation intercalation by intercalating different cations. Compared to Na^+ and K^+, the insertion of Li^+ tends to achieve better electrochemical performance and capacitance behavior. Nb_2CT_x electrode in the Li_2SO_4 electrolyte shows a higher specific capacitance of 120 F/g at 20 mV/s, due to the fast transport and easy intercalation of the small-sized Li^+ between Nb_2CT_x layers.

Hybrid capacitors, with battery-type and capacitive-type materials as electrodes, can take into consideration high power density of supercapacitors as well as high energy density of batteries. Recently, the application of Nb_2CT_x in hybrid capacitors has attracted extensive attention. As shown in Figure 10a, Qin et al. [112] have prepared single-crystal perovskite $NaNbO_3$ nanocubes (S-P-NNO NCs) using a hydrothermal alkalization method with few-layer Nb_2CT_x (f-Nb_2CT_x). The f-Nb_2CT_x and S-P-NNO NCs are further assembled via freeze-drying to obtain S-P-NNO/f-Nb_2CT_x composites. Benefiting from the 3D-connected porous conductive network (Figure 10b) and synergistic effect between f-Nb_2CT_x and S-P-NNO NCs, the composites in Lithium-ion capacitors (LICs), shows a capacity of 157 mAh/g at 2.0 A/g (Figure 10c) and an energy density of 56 Wh/kg at the power density of 13 kW/kg in a full hybrid cell (Figure 10d).

At present, the experimental conditions of research on Nb_2CT_x are relatively mild and are mainly focused on aqueous electrolyte. Since the electrochemical stability of Nb_2CT_x MXene is relatively poor, designing a stable structure and optimizing application conditions to inhibit the oxidation and dissolution of Nb_2CT_x are also necessary.

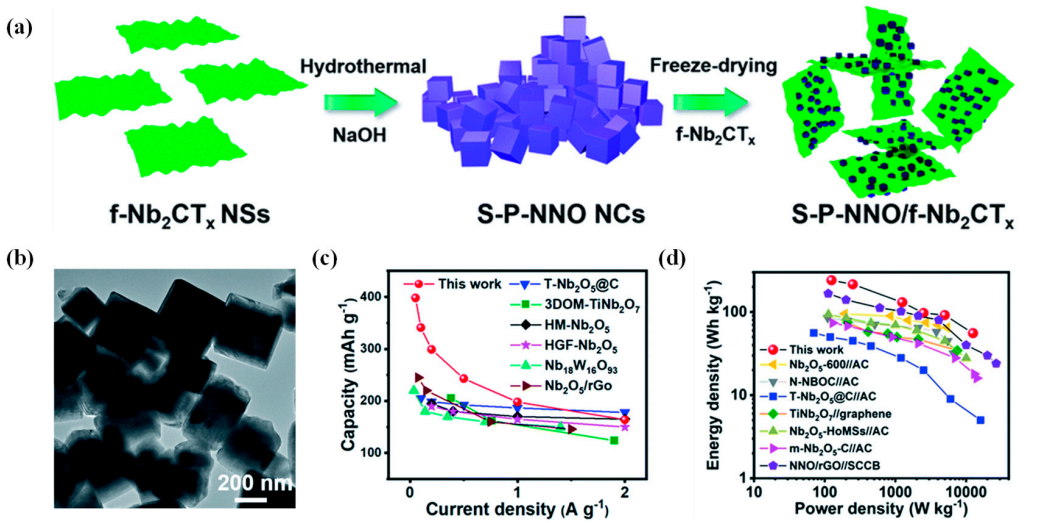

Figure 10. Applications of Nb_2CT_x in hybrid supercapacitors. (**a**) Schematic illustration of the synthetic process of the S-P-NNO/f-Nb_2CT_x, (**b**) TEM image of S-P-NNO/f-Nb_2CT_x, (**c**) Rate properties of S-P-NNO/f-Nb_2CT_x and other Nb-based oxide anodes, (**d**) Ragone plots of S- P-NNO/f-Nb_2CT_x for LICs. Copyright Royal Society of Chemistry, 2021 [112].

4.3. Electrocatalytic Hydrogen Evolution

Electrocatalytic hydrogen evolution reaction (HER) is an important clean and efficient hydrogen production method, as hydrogen is considered to be an effective substitute for traditional fossil fuels [113,114]. Recent studies have proven that MXene-based catalysts have potential application in HER [115], or the -O functional groups on MXene surface are the active sites for HER [116]. Figure 11a provides a volcano map of the theoretical exchange current and the average Gibbs free energy of hydrogen adsorption. The predictions have shown that, the high binding strength of Nb_2CO_2 and H leads to a slightly poorer HER catalytic performance than that of $Ti_3C_2O_2$ [17]. Currently, some studies are devoted to weakening the hydrogen adsorption of Nb_2CT_x and improving the electrocatalytic hydrogen evolution activity.

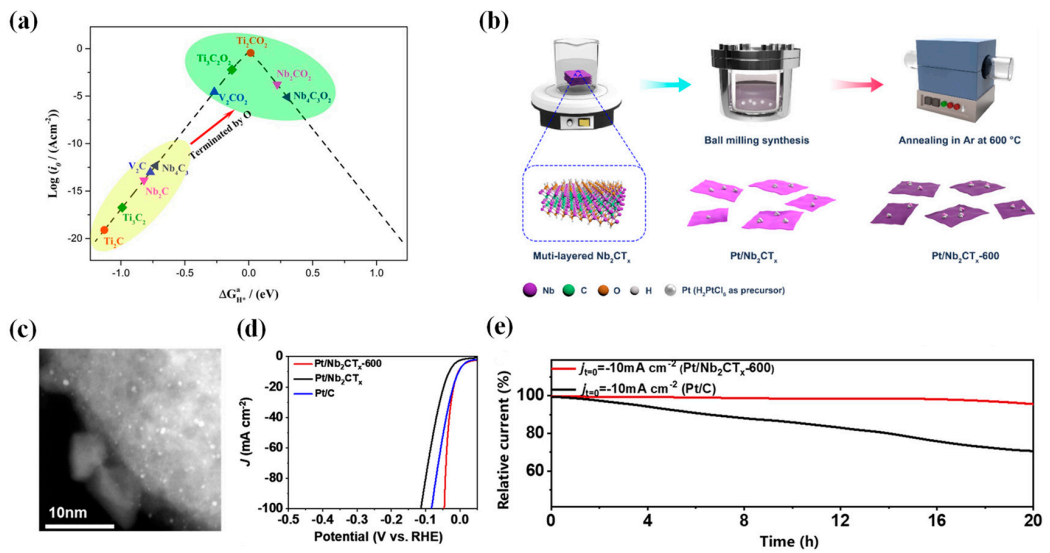

Figure 11. Applications of Nb_2CT_x in electrocatalytic hydrogen evolution reaction. (**a**) Volcano curve of exchange current (i_0) as a function of the average Gibbs free energy of hydrogen adsorption (ΔG^a_{H*}). Copyright American Chemical Society, 2016 [17]. (**b**) Schematic illustration of the preparation of Pt/Nb_2CT_x-600 catalyst, (**c**) TEM image of Pt/Nb_2CT_x-600, (**d**) Electrocatalytic HER performance of Pt/Nb_2CT_x-600 in 0.5 M H_2SO_4, (**e**) CA curves of Pt/Nb_2CT_x-600 and Pt/C catalysts for HER performance. Copyright MDPI, 2021 [116].

Anchoring single transition metal atom into 2D materials is an important strategy to develop electrocatalysts with high HER performance. As shown in Figure 11b, Fan et al. [117] have immobilized platinum nanoclusters on Nb_2CT_x via mechanochemical ball milling method to get electrocatalysts for hydrogen evolution. Ultrafine Pt_3Nb nanoclusters are formed on the Pt/Nb_2CT_x composite after annealing at 600 °C (Figure 11c) and the average diameter of Pt_3Nb nanoclusters is 1.5 nm. The Pt/Nb_2CT_x-600 demonstrates a low overpotential of 46 mV and 5 mV at the current density of 100 mA/cm^2 and 10 mA/cm^2, respectively (Figure 11d). After 20 h test, the Pt/Nb_2CT_x-600 also shows 5% degradation (Figure 11e). The good HER property can be attributed to more active sites and homogenous Pt dispersion after the thermal treatment and mechanochemical process. Zhang et al. [118] have studied the effect of surface functionalization of Nb_2CT_x-supported Pd catalysts for HER performance. Compared with oxygen-rich materials, the F-rich Nb_2CT_x-based Pd nanocatalyst shows better HER property and long-term stability. The Pd/Nb_2C-HF shows an overpotential of 34 mV at 10 mA/cm^2, with the Tafel slope of 34 mV/dec. The improved HER property of Pd/Nb_2C with F-rich terminated catalyst can be attributed to the weakened adsorption of hydrogen, which make the evolution of hydrogen easier. Zhao et al. [23] have anchored Co single atoms on Nb_2CT_x to obtain Co@ Nb_2CT_x composites. Because of the stronger hybridization between surface-terminated O_{2p} orbitals of Nb_2CT_x and Co_{3d} orbitals, the Co atoms in the Co@ Nb_2CT_x have an optimized electronic structure, leading a lower HER energy barriers and accelerated catalytic kinetics.

Except for anchoring transition metals, other strategies to prepare effective catalysts are also adopted. Jiang et al. [24] have tailored 2D Nb_2CT_x nanosheets into quantum dots (QDs), with active sites at the Nb_2CT_x QDs edges enriched. The intermediate H* (absorbed hydrogen) species can be more moderately bound with metal atoms at the edge of Nb_2CT_x QDs, delivering a lower energy barrier. Nb_2CT_x QDs exhibits 6.8 times higher activity than pure Nb_2CT_x nanosheets and has good stability.

4.4. Photocatalytic H_2 Evolution

Nb_2CT_x is an ideal candidate for photocatalyst because of its rich functional groups, hierarchical lamellar structure and good photocatalytic properties.

As shown in Figure 12a, Huang et al. [64] have prepared 2D CdS/2D Nb_2CT_x composite using the electrostatic self-assembly and solvothermal reaction. After the hydrothermal reaction of 2D CdS with Nb_2CT_x, the 2D CdS nanosheets will cover Nb_2CT_x, and form a flower-like morphology (Figure 12b). The photocatalytic H_2 evolution rate of CdS/Nb_2CT_x composite is about 5040 μmol/g/h, which is 4.3 times higher than that of pure 2D CdS (Figure 12c). In CdS/Nb_2CT_x composite, Schottky heterojunction formed can the redistribution of charges on this 2D CdS/2D Nb_2CT_x composite and accelerate the photo-generated charge separation and transfer of 2D CdS nanosheets, thus to promote the water splitting reaction with more photo-generated electrons. Cui et al. [16] have synthesized ultrathin Bi_2WO_6/Nb_2CT_x composite photocatalyst using the hydrothermal method. The Nb_2CT_x flakes can greatly improve the separation efficiency of photogenerated carriers and boost the photocatalytic activity of Bi_2WO_6. Through in situ calcination, Makola et al. [119] have prepared a metal-free Nb_2CT_x@g-C_3N_4 Schottky junction photocatalyst. The heterostructure exhibits a narrow energy bandgap and can significantly suppress electron recombination rate, indicating potential application in the photocatalytic. Peng et al. [25] have synthesized Nb_2O_5 nanorod arrays on Nb_2CT_x nanosheets via hydrothermal method, followed by photodepositing Ag nanoparticles to form hierarchical composites. The Ag/Nb_2O_5@Nb_2CT_x nanohybrid exhibits 3.6 times higher photocatalytic H_2 evolution rate than Nb_2O_5 nanoparticles. The performance can be explained using the photogeneration efficient of electron-hole pairs provided by Nb_2O_5 nanorods and abundant active sites provided by Ag nanoparticles. Tayyab et al. [120] have synthesized $In_2S_3/Nb_2O_5/Nb_2C$ (INNC) via a one-pot in situ hydrothermal method. During the hydrothermal process, Nb_2CT_x flakes are partial oxidized into Nb_2O_5 nanorods, and In_2S_3 nanoparticles are chemically anchored on Nb_2CT_x flakes and Nb_2O_5 nanorods. Due

to the heterojunction of In_2S_3/ Nb_2O_5, INNC composite has an improved photoexcited charge carrier transfer with a higher photocatalytic H_2 evolution rate (68.8 μmol/g/h) than Nb_2O_5/Nb_2C or In_2S_3. Xu et al. [121] have synthesized Ru/Nb_2O_5@Nb_2C using one-pot method. During the hydrothermal reaction, Nb_2C is partially oxidized into semiconductor Nb_2O_5 nanowires and Ru^{3+} is reduced to Ru on Nb_2O_5/Nb_2C in the deposition process. The Ru/Nb_2O_5@Nb_2C with metal/semiconductor/Nb_2CT_x MXene heterojunction has a reduced photo-generated carrier transfer resistance, showing improved photocatalytic HER performance of 10.11 mmol/g/h.

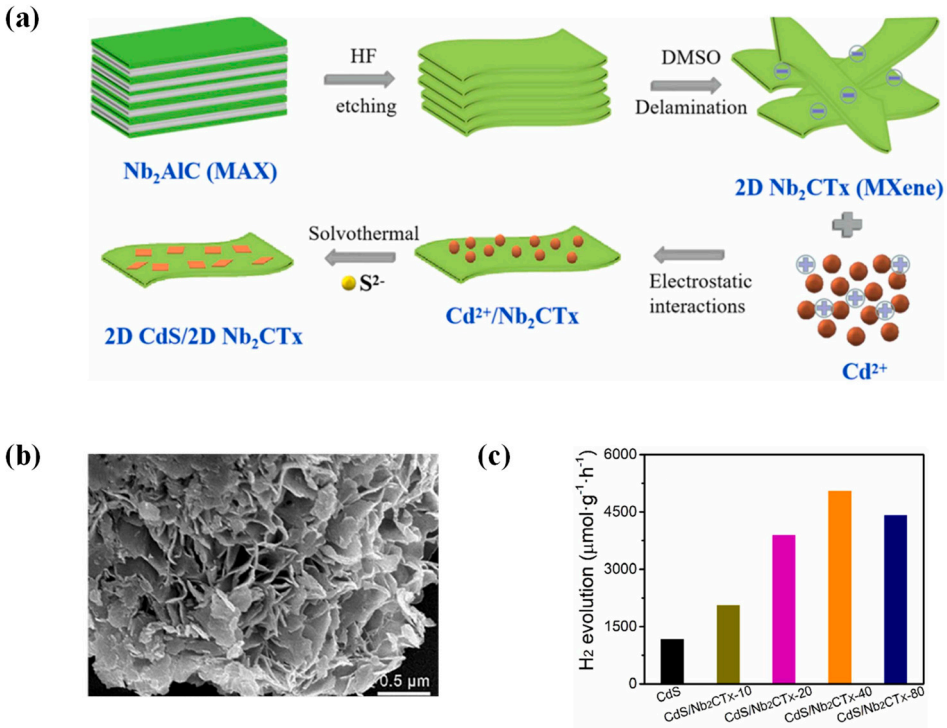

Figure 12. Applications of Nb_2CT_x in photocatalyst. (**a**) Schematic illustration of fabrication procedure of CdS/Nb_2CT_x, (**b**) SEM image of CdS/Nb_2CT_x-40, (**c**) Photocatalytic H_2 evolution rates of CdS and CdS/Nb2CTx. Copyright Elsevier, 2022 [64].

The photocatalytic H_2 evolution performance of Nb_2CT_x and its composites are listed in Table 4.

Table 4. The specific capacities of Nb_2CT_x for Photocatalytic H_2 evolution.

Materials	H_2 Production (μmol/g/h)	Sacrificial Reagent	References
Ag/Nb_2O_5@Nb_2CT_x	824.2	Methanol	[25]
1D CdS/2D Nb_2CT_x	5300	Lactic acid (10 vol%)	[26]
2D CdS/2D Nb_2CT_x	5040	Lactic acid (10 vol%)	[64]
In_2S_3/Nb_2O_5/Nb_2C	68.8	Methanol	[120]
Ru/Nb_2O_5@Nb_2C	10,110	Methanol	[121]

4.5. Sensors

MXene is also widely applied in sensing because of high conductivity, rich functional groups and high hydrophilicity. Nb_2CT_x, as another typical member of MXene family, has also generated wide interests for its potential use in sensors in recent years.

Zhao et al. [61] have designed an electrospinning neuron-like Nb_2CT_x/SA composite film, used as self-powered humidity sensors. The composite film can provide many nanochannels and adsorption sites for the directional ionization and transfer of water molecules. The moist-electric humidity sensor (MEHS) of Nb_2CT_x/SA composite shows

fast response/recovery time, good long-term cycle stability, linearity, repeatability as well as low detection limit. Bi et al. [18] have studied the Nb_2CT_x in relative humidity (RH) measurement (Figure 13a). Microfibers and Nb_2CT_x are integrated using optical deposition for fiber-optic-based RH sensing. The RH sensing experiments show that as the RH levels increase from 18.5% to 72.4%, the transmission spectra (Figure 13b) initially blue shift with the sensitivity of −86 pm/% RH because of the change in effective refractive index of Nb_2CT_x. The transmission spectra (Figure 13c) exhibit a red shift in the RH from 72.4% to 95.4% RH, and the sensitivity is 585 pm/% RH due to the variations in Nb_2CT_x structure.

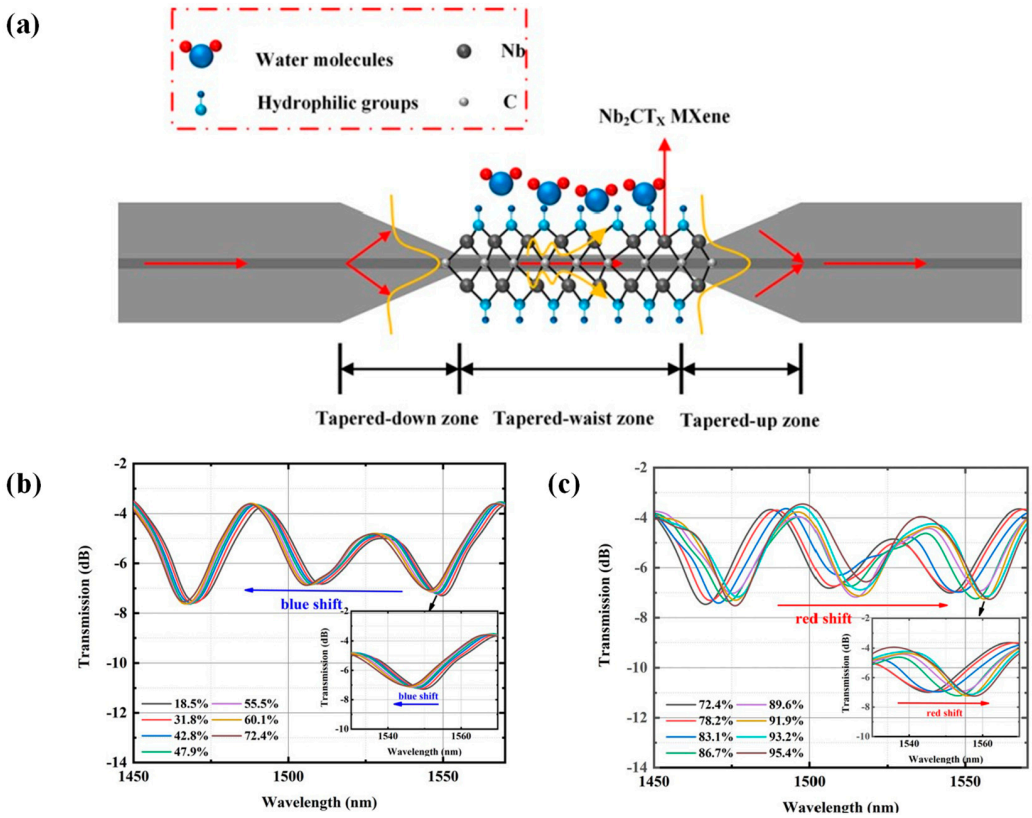

Figure 13. Applications of Nb_2CT_x in sensors. (**a**) Schematic diagram of the Nb2CTx nanosheet-coated microfiber RH sensor, (**b**) Transmission spectra in the RH range of 18.5–72.4% RH, (**c**) Transmission spectra in the RH range of 72.4–95.4% RH. Copyright American Institute of Physics, 2022 [18].

Li et al. [122] have synthesized a new heterogeneous convex fiber-tapered seven core fiber-convex fiber (CTC) probe via Nb_2CT_x, gold nanoparticles (AuNPs) and creatinase (CA) enzyme. The probe, combined with localized surface plasmon resonance (LSPR) technology, is used to test the concentration of creatinine. Since strong evanescent fields can induce the LSPR effect and stimulate AuNPs, the sensitivity of this probe increases. This sensor has a sensitivity of 3.1 pm/μM as well as limit of detection, which is 86.12 μM at the linear from 0 to 2000 μM. Wang et al. [28] have prepared a novel Nb_2CT_x/PANI sensor to efficiently detect NH_3 (Figure 14a). The gas-sensing response of the Nb_2CT_x/PANI-2 sensor (301.31%) is about 2.34 times higher than PANI sensor (128.81%), upto 100 ppm NH_3 under 87.1% RH (Figure 14b). The p-n junction is favorable to the enhancement of the gas-sensing properties of the Nb_2CT_x/PANI sensor.

In addition to the above applications, Nb_2CT_x sensors are also used for water quality monitoring [29], NO_2 gas detection [123], fluorescence detection of heavy metal ions [27], biosensing application [56], and detection of human hemoglobin concentration [124], etc.

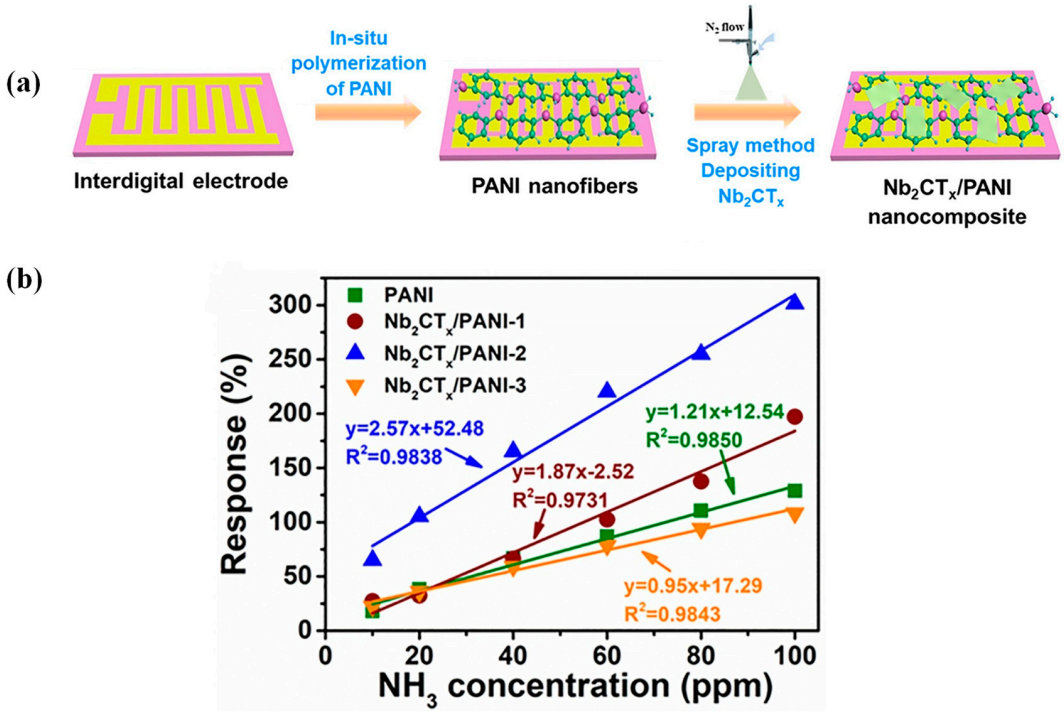

Figure 14. (**a**) Schematic illustration of fabrication process of the Nb_2CT_x/PANI sensor, (**b**) Response–concentration fitting curves of the PANI, Nb_2CT_x/PANI-1, Nb_2CT_x/PANI-2 and Nb_2CT_x/PANI-3 sensors toward 10–100 ppm NH_3. Copyright Elsevier, 2020 [28].

4.6. Other Applications

4.6.1. Electromagnetic Interference (EMI) Shielding and Microwave Absorption (MA)

Nb_2CT_x is used in EMI shielding because of its unique structure, special metallic properties and abundant natural defects [33,125,126]. Rajavel et al. [126] have prepared a mixed composite of lamellar-structured Nb_2CT_x and one-step-extracted low-stratified Nb_2CT_x for EMI shielding. The composite material shows good EMI shielding efficiency of 44.09 $\pm$ 1.99 dB at 12 GHz. Similarly, Nb_2CT_x has also been used for microwave absorption (MA) [127,128]. Song et al. [119] have synthesized Nb_2O_5/ Nb_2CT_x hybrids using microwave-assisted hydrothermal method. The hybrids shows good microwave absorption performance and a minimum reflection loss (RL) vof -44.1 dB at 2.8 GHz with the thickness of 5 mm.

4.6.2. Photodetector

Zhang et al. [67] have grown Bi NPs on the Nb_2CT_x surface to prepare Nb_2CT_x@Bi Schottky heterojunction. The Nb_2CT_x@Bi flexible photodetector has unique self-powered photodetection capability, and the response and recovery speed is both 0.08 s. In addition, Nb_2CT_x@Bi shows a specific detectivity of 4.63×10^{12} Jones and a responsivity of 585.25 mA/W. Because of the reduced charge transmission time as well as the Schottky barrier and built-in electric field at the interface of Bi and Nb_2CT_x, the uniflow spreading process of electrons is accelerated, the separation of photo-induced electron/hole pairs is facilitated and carrier recombination dynamics is hindered. Therefore, Nb_2CT_x@Bi shows improved photodetection capability.

4.6.3. Perovskite Solar Cells (PVSCs)

Due to adjustable optoelectrical properties and numerous surface functional groups, Nb_2CT_x has also been used in Perovskite solar cells [30,129]. Zhang et al. [129] have reduced the work function (WF) by replacing -F groups with -NH_2 groups via hydrazine treatment and obtained T-Nb_2CT_x. The T-Nb_2CT_x electron transport layer (ETL) shows outstanding optoelectrical properties, highly matched energy level with perovskite layer,

high transmittance and conductivity. After incorporating T-Nb_2CT_x into the perovskite precursor, hydrogen bond with iodine ions is formed to retard the crystallization rate. The T-Nb_2CT_x as ETL achieves a high power conversion efficiency (PCE) of 21.79% with good stability.

In addition to the above applications, Nb_2CT_x is also used in nitrogen reduction reaction (NRR) catalysts [130], dye adsorption [34], solar-driven water evaporation [131], H_2O_2 synthesis catalysts and organic dyes degradation [132].

5. Summary and Outlook

This review has summarized the synthesis and properties of Nb_2CT_x as well as its different applications in secondary batteries, supercapacitors, electrocatalysis and sensing. The wide application of Nb_2CT_x is attributed to its high conductivity, high theoretical specific capacity, abundant functional groups and high hydrophilicity. At present, the study of Nb_2CT_x is at the preliminary stage, as there are many challenges related to synthesis, properties and application which should be fixed before it can be studied further. This review also deals with some potential application such as EMI, MA and photodetector, that needs to be focused on.

In terms of synthesis, Nb_2CT_x is etched using mainly acid etching methods, especially the high concentration HF etching method, which is effective but harmful to the humans and the environment. Therefore, exploring fluorine-free etching methods is essential. Both molten salt etching and electrochemical etching have been reported as fluorine-free etching methods, but the experimental conditions and parameter details of these methods still need to be fully discussed. In addition, the delamination of Nb_2CT_x is a necessary step to get single-layer or few-layer Nb_2CT_x nanosheets. Most of the intercalation currently used are organic bases, such as TMAOH and TPAOH. Nonetheless, further exploration is needed to develop low-cost and harmless intercalants.

Because of the Van der Waals force between Nb_2CT_x sheets, Nb_2CT_x nanosheets tend to be aggregated or restacked to form a dense structure, sacrificing the specific surface area and active sites. When using as an electrode in energy storage, it will lead to poorer cycling stability, lower specific capacitance value and rate capability. Therefore, more work should be carried out to suppress the self-stacking of Nb_2CT_x in order to increase the specific surface area, provide more active sites, and optimize the electrochemical utilization of Nb_2CT_x.

Treatment of surface functional groups (alkali treatment or heat treatment) is an effective way to tune the property of Nb_2CT_x. Specially, increasing -O functional groups and reducing -F functional groups on Nb_2CT_x can greatly improve the electrochemical performance. Studies have shown that after treating with alkali (KOH, LiOH) or transition metal salts ($CuSO_4$, $FeSO_4$), the Nb_2CT_x or Nb_2CT_x composites tends to form a porous structure, with increasing specific surface area and more active sites. It is found that introducing carbon materials (CNTs and CQDs), conductive polymers, metal oxides or other metal cations into the Nb_2CT_x layers can affect the interlayer spacing of Nb_2CT_x, inhibiting the self-stacking of Nb_2CT_x. In addition, single-atom doping, designing heterostructures, and constructing 3D porous structures are also effective methods to improve the electrochemical reaction active sites and enhance the electrochemical performance.

In terms of application, Nb_2CT_x is widely used in secondary batteries and supercapacitors. However, the mechanism of charge storage needs to be studied more in order to lay a solid foundation to guide future research or commercial application. Moreover, at present, there is no research on some areas of Nb_2CT_x applications. For example, aqueous zinc metal (Zn^0) batteries (LAMBs) are among the most promising beyond-lithium technologies [133]. However, not many studies have been conducted to assess the application of Nb_2CT_x in LAMBs and as such it needs to be further carried out and developed. Additionally, application of Nb_2CT_x in the fields of biology, medicine, photoelectric detection and electromagnetic shielding also need more attention and effort.

Author Contributions: Conceptualization, methodology, resources, data curation, writing, draft preparation, G.G. Supervision, project administration, funding acquisition and revision, F.G. All authors have read and agreed to the published version of the manuscript.

Funding: This work was funded by the National Natural Science Foundation of China, grant number 52002354, and China Postdoctoral Science Foundation, grant number 2020M672256.

Data Availability Statement: No new data were created or analyzed in this study. Data sharing is not applicable to this article.

Conflicts of Interest: The authors declare no conflict of interest.

References

1. Yi, S.; Wang, L.; Zhang, X.; Li, C.; Liu, W.; Wang, K.; Sun, X.; Xu, Y.; Yang, Z.; Cao, Y.; et al. Cationic intermediates assisted self-assembly two-dimensional $Ti_3C_2T_x$/rGO hybrid nanoflakes for advanced lithium-ion capacitors. *Sci. Bull.* **2021**, *66*, 914–924. [CrossRef]
2. Yang, K.; Luo, M.; Zhang, D.; Liu, C.; Li, Z.; Wang, L.; Chen, W.; Zhou, X. $Ti_3C_2T_x$/carbon nanotube/porous carbon film for flexible supercapacitor. *Chem. Eng. J.* **2022**, *427*, 132002. [CrossRef]
3. Fan, Z.; Yang, Y.; Ma, H.; Wang, Y.; Xie, Z.; Liu, Y. High-volumetric capacitance and high-rate performance in liquid-mediated densified holey MXene film. *Carbon* **2022**, *186*, 150–159. [CrossRef]
4. Huang, P.; Zhang, S.; Ying, H.; Yang, W.; Wang, J.; Guo, R.; Han, W. Fabrication of Fe nanocomplex pillared few-layered $Ti_3C_2T_x$ MXene with enhanced rate performance for lithium-ion batteries. *Nano Res.* **2020**, *14*, 1218–1227. [CrossRef]
5. You, Q.; Guo, Z.; Zhang, R.; Chang, Z.; Ge, M.; Mei, Q.; Dong, W.F. Simultaneous Recognition of Dopamine and Uric Acid in the Presence of Ascorbic Acid via an Intercalated MXene/PPy Nanocomposite. *Sensors* **2021**, *21*, 3069. [CrossRef] [PubMed]
6. Wu, W.; Zhao, C.; Niu, D.; Zhu, J.; Wei, D.; Wang, C.; Wang, L.; Yang, L. Ultrathin N-doped Ti_3C_2-MXene decorated with $NiCo_2S_4$ nanosheets as advanced electrodes for supercapacitors. *Appl. Surf. Sci.* **2021**, *539*, 148272. [CrossRef]
7. Yang, S.; Zhang, P.; Nia, A.S.; Feng, X. Emerging 2D Materials Produced via Electrochemistry. *Adv. Mater.* **2020**, *32*, e1907857. [CrossRef]
8. Liu, M.; Li, J.; Bian, R.; Wang, X.; Ji, Y.; Zhang, X.; Tian, J.; Shi, F.; Cui, H. ZnO@Ti_3C_2 MXene interfacial Schottky junction for boosting spatial charge separation in photocatalytic degradation. *J. Alloys Compd.* **2022**, *905*, 164025. [CrossRef]
9. Liu, M.; Ji, J.; Song, P.; Wang, J.; Wang, Q. Sensing performance of α-Fe_2O_3/ $Ti_3C_2T_x$ MXene nanocomposites to NH_3 at room temperature. *J. Alloys Compd.* **2022**, *898*, 162812. [CrossRef]
10. Yun, T.; Kim, H.; Iqbal, A.; Cho, Y.S.; Lee, G.S.; Kim, M.K.; Kim, S.J.; Kim, D.; Gogotsi, Y.; Kim, S.O.; et al. Electromagnetic Shielding of Monolayer MXene Assemblies. *Adv. Mater.* **2020**, *32*, e1906769. [CrossRef]
11. Su, T.; Peng, R.; Hood, Z.D.; Naguib, M.; Ivanov, I.N.; Keum, J.K.; Qin, Z.; Guo, Z.; Wu, Z. One-Step Synthesis of Nb_2O_5/C/Nb_2C (MXene) Composites and Their Use as Photocatalysts for Hydrogen Evolution. *ChemSusChem* **2018**, *11*, 688–699. [CrossRef]
12. Ren, X.; Huo, M.; Wang, M.; Lin, H.; Zhang, X.; Yin, J.; Chen, Y.; Chen, H. Highly Catalytic Niobium Carbide (MXene) Promotes Hematopoietic Recovery after Radiation by Free Radical Scavenging. *ACS Nano* **2019**, *13*, 6438–6454. [CrossRef] [PubMed]
13. Cheng, R.; Hu, T.; Wang, Z.; Yang, J.; Dai, R.; Wang, W.; Cui, C.; Liang, Y.; Zhang, C.; Li, C.; et al. Understanding charge storage in Nb_2CT_x MXene as an anode material for lithium ion batteries. *Phys. Chem. Chem. Phys.* **2021**, *23*, 23173–23183. [CrossRef]
14. Zhao, J.; Wen, J.; Xiao, J.; Ma, X.; Gao, J.; Bai, L.; Gao, H.; Zhang, X.; Zhang, Z. Nb_2CT_x MXene: High capacity and ultra-long cycle capability for lithium-ion battery by regulation of functional groups. *J. Energy Chem.* **2021**, *53*, 387–395. [CrossRef]
15. Xin, Y.; Yu, Y.-X. Possibility of bare and functionalized niobium carbide MXenes for electrode materials of supercapacitors and field emitters. *Mater. Des.* **2017**, *130*, 512–520. [CrossRef]
16. Cui, C.; Guo, R.; Xiao, H.; Ren, E.; Song, Q.; Xiang, C.; Lai, X.; Lan, J.; Jiang, S. Bi_2WO_6/Nb_2CT_x MXene hybrid nanosheets with enhanced visible-light-driven photocatalytic activity for organic pollutants degradation. *Appl. Surf. Sci.* **2020**, *505*, 144595. [CrossRef]
17. Gao, G.; O'Mullane, A.P.; Du, A. 2D MXenes: A New Family of Promising Catalysts for the Hydrogen Evolution Reaction. *ACS Catal.* **2016**, *7*, 494–500. [CrossRef]
18. Bi, M.; Miao, Y.; Li, W.; Yao, J. Niobium carbide MXene-optics fiber-sensor for high sensitivity humidity detection. *Appl. Phys. Lett.* **2022**, *120*, 021103. [CrossRef]
19. Lee, S.H.; Kim, M.S.; Lee, J.-H.; Ryu, J.-H.; Do, V.; Lee, B.G.; Kim, W.; Cho, W.I. A Li–In alloy anode and Nb_2CT_x artificial solid-electrolyte interphase for practical Li metal batteries. *J. Mater. Chem. A* **2022**, *10*, 4157–4169. [CrossRef]
20. Mashtalir, O.; Lukatskaya, M.R.; Zhao, M.Q.; Barsoum, M.W.; Gogotsi, Y. Amine-Assisted Delamination of Nb_2C MXene for Li-Ion Energy Storage Devices. *Adv. Mater.* **2015**, *27*, 3501–3506. [CrossRef]
21. Mao, T.; Zhou, F.; Han, K.; Xie, Y.; Wang, J.; Wang, L. Self-standing reduced graphene oxide/Nb_2C MXene paper electrode with three-dimensional open structure for high-rate potassium ion storage. *J. Phys. Chem. Solids* **2022**, *169*, 110838. [CrossRef]
22. Li, K.; Zhao, J.; Zhussupbekova, A.; Shuck, C.E.; Hughes, L.; Dong, Y.; Barwich, S.; Vaesen, S.; Shvets, I.V.; Mobius, M.; et al. 4D printing of MXene hydrogels for high-efficiency pseudocapacitive energy storage. *Nat. Commun.* **2022**, *13*, 6884. [CrossRef] [PubMed]
23. Zhao, X.; Zheng, X.; Lu, Q.; Li, Y.; Xiao, F.; Tang, B.; Wang, S.; Yu, D.Y.W.; Rogach, A.L. Electrocatalytic enhancement mechanism of cobalt single atoms anchored on different MXene substrates in oxygen and hydrogen evolution reactions. *EcoMat* **2022**, *5*, e12293. [CrossRef]

24. Jiang, B.; Yang, T.; Wang, T.; Chen, C.; Yang, M.; Yang, X.; Zhang, J.; Kou, Z. Edge stimulated hydrogen evolution reaction on monodispersed MXene quantum dots. *Chem. Eng. J.* **2022**, *442*, 136119. [CrossRef]
25. Peng, C.; Xie, X.; Xu, W.; Zhou, T.; Wei, P.; Jia, J.; Zhang, K.; Cao, Y.; Wang, H.; Peng, F.; et al. Engineering highly active Ag/Nb_2O_5@Nb_2CT_x (MXene) photocatalysts via steering charge kinetics strategy. *Chem. Eng. J.* **2021**, *421*, 128766. [CrossRef]
26. Huang, J.; Tao, J.; Liu, G.; Lu, L.; Tang, H.; Qiao, G. In situ construction of 1D CdS/2D Nb_2CT_x MXene Schottky heterojunction for enhanced photocatalytic hydrogen production activity. *Appl. Surf. Sci.* **2022**, *573*, 151491. [CrossRef]
27. Yang, G.; Zhao, J.; Yi, S.; Wan, X.; Tang, J. Biodegradable and photostable Nb_2C MXene quantum dots as promising nanofluorophores for metal ions sensing and fluorescence imaging. *Sens. Actuators B Chem.* **2020**, *309*, 127735. [CrossRef]
28. Wang, S.; Liu, B.; Duan, Z.; Zhao, Q.; Zhang, Y.; Xie, G.; Jiang, Y.; Li, S.; Tai, H. PANI nanofibers-supported Nb_2CT_x nanosheets-enabled selective NH_3 detection driven by TENG at room temperature. *Sens. Actuators B Chem.* **2021**, *327*, 128923. [CrossRef]
29. Bi, M.; Miao, Y.; Li, W.; Fei, C.; Zhang, K. Ultrasensitive BOD Detection of Fiber Integrated With Nb_2CT_x MXene for Water Pollution. *J. Light. Technol.* **2022**, *40*, 2173–2180. [CrossRef]
30. Qamar, S.; Fatima, K.; Ullah, N.; Akhter, Z.; Waseem, A.; Sultan, M. Recent progress in use of MXene in perovskite solar cells: For interfacial modification, work-function tuning and additive engineering. *Nanoscale* **2022**, *14*, 13018–13039. [CrossRef]
31. Liu, Z.; El-Demellawi, J.K.; Bakr, O.M.; Ooi, B.S.; Alshareef, H.N. Plasmonic Nb_2CT_x MXene-$MAPbI_3$ Heterostructure for Self-Powered Visible-NIR Photodiodes. *ACS Nano* **2022**, *16*, 7904–7914. [CrossRef]
32. Yin, J.; Pan, S.; Guo, X.; Gao, Y.; Zhu, D.; Yang, Q.; Gao, J.; Zhang, C.; Chen, Y. Nb_2C MXene-Functionalized Scaffolds Enables Osteosarcoma Phototherapy and Angiogenesis/Osteogenesis of Bone Defects. *Nanomicro Lett.* **2021**, *13*, 30. [CrossRef]
33. Rajavel, K.; Hu, Y.; Zhu, P.; Sun, R.; Wong, C. MXene/metal oxides-Ag ternary nanostructures for electromagnetic interference shielding. *Chem. Eng. J.* **2020**, *399*, 125791. [CrossRef]
34. Yan, Y.; Han, H.; Dai, Y.; Zhu, H.; Liu, W.; Tang, X.; Gan, W.; Li, H. Nb_2CT_x MXene Nanosheets for Dye Adsorption. *ACS Appl. Nano Mater.* **2021**, *4*, 11763–11769. [CrossRef]
35. Naguib, M.; Mochalin, V.N.; Barsoum, M.W.; Gogotsi, Y. 25th anniversary article: MXenes: A new family of two-dimensional materials. *Adv. Mater.* **2014**, *26*, 992–1005. [CrossRef] [PubMed]
36. Huang, C.; Shi, S.; Yu, H. Work Function Adjustment of Nb_2CT_x Nanoflakes as Hole and Electron Transport Layers in Organic Solar Cells by Controlling Surface Functional Groups. *ACS Energy Lett.* **2021**, *6*, 3464–3472. [CrossRef]
37. Wang, Y.C.; Liang, Z.H.; Peng, G.H.; Xu, J.G. Synthesis of Nb_2AlC Material by High Temperature Solid State Reaction Method. *Key Eng. Mater.* **2015**, *655*, 240–243. [CrossRef]
38. Stumpf, M.; Biggemann, J.; Fey, T.; Kakimoto, K.I.; Greil, P. Nb_2AlC particle reinforced ZrO_2-matrix composites. *J. Ceram. Sci. Tech.* **2018**, *9*, 271–278.
39. Stumpf, M.; Biggemann, J.; Fey, T.; Kakimoto, K.-i.; Greil, P. Thermochemical calculations of the oxidation behavior of Nb_2AlC MAX phase in ZrO_2–matrix composites. *Ceram. Int.* **2018**, *44*, 15747–15753. [CrossRef]
40. Stumpf, M.; Fey, T.; Kakimoto, K.-I.; Greil, P. Nb_2AlC-particle induced accelerated crack healing in ZrO_2–matrix composites. *Ceram. Int.* **2018**, *44*, 19352–19361. [CrossRef]
41. Yeh, C.L.; Kuo, C.W. An investigation on formation of Nb_2AlC by combustion synthesis of Nb_2O_5–Al–Al_4C_3 powder compacts. *J. Alloys Compd.* **2010**, *496*, 566–571. [CrossRef]
42. Levashov, E.A.; Mukasyan, A.S.; Rogachev, A.S.; Shtansky, D.V. Self-propagating high-temperature synthesis of advanced materials and coatings. *Int. Mater. Rev.* **2016**, *62*, 203–239. [CrossRef]
43. Kovalev, I.D.; Miloserdov, P.A.; Gorshkov, V.A.; Kovalev, D.Y. Synthesis of Nb_2AlC MAX Phase by SHS Metallurgy. *Russ. J. Non-Ferr. Met.* **2020**, *61*, 126–131. [CrossRef]
44. Afanasyev, N.I.; Lepakova, O.K.; Kitler, V.D. Non-isothermal synthesis of materials based on the MAX phases in the Ti-Si-C and Nb-Al-C systems. *J. Phys. Conf. Ser.* **2020**, *1459*, 012008. [CrossRef]
45. Zhou, W.; Li, K.; Zhu, J.; Tian, S. Rapid synthesis of highly pure Nb_2AlC using the spark plasma sintering technique. *J. Phys. Chem. Solids* **2018**, *120*, 218–222. [CrossRef]
46. Zhao, J.; Wen, J.; Bai, L.; Xiao, J.; Zheng, R.; Shan, X.; Li, L.; Gao, H.; Zhang, X. One-step synthesis of few-layer niobium carbide MXene as a promising anode material for high-rate lithium ion batteries. *Dalton Trans.* **2019**, *48*, 14433–14439. [CrossRef]
47. Zaheer, A.; Zahra, S.A.; Iqbal, M.Z.; Mahmood, A.; Khan, S.A.; Rizwan, S. Nickel-adsorbed two-dimensional Nb_2C MXene for enhanced energy storage applications. *RSC Adv.* **2022**, *12*, 4624–4634. [CrossRef]
48. Feng, Y.; He, M.; Liu, X.; Wang, W.; Yu, A.; Wan, L.; Zhai, J. Alternate-Layered MXene Composite Film-Based Triboelectric Nanogenerator with Enhanced Electrical Performance. *Nanoscale Res. Lett.* **2021**, *16*, 81. [CrossRef]
49. Pandey, R.P.; Rasheed, P.A.; Gomez, T.; Rasool, K.; Ponraj, J.; Prenger, K.; Naguib, M.; Mahmoud, K.A. Effect of Sheet Size and Atomic Structure on the Antibacterial Activity of Nb-MXene Nanosheets. *ACS Appl. Nano Mater.* **2020**, *3*, 11372–11382. [CrossRef]
50. Jiang, Y.; Tian, M.; Wang, H.; Wei, C.; Sun, Z.; Rummeli, M.H.; Strasser, P.; Sun, J.; Yang, R. Mildly Oxidized MXene (Ti_3C_2, Nb_2C, and V_2C) Electrocatalyst via a Generic Strategy Enables Longevous Li-O_2 Battery under a High Rate. *ACS Nano* **2021**, *15*, 19640–19650. [CrossRef]
51. Xiao, J.; Zhao, J.; Ma, X.; Li, L.; Su, H.; Zhang, X.; Gao, H. One-step synthesis Nb_2CT_x MXene with excellent lithium-ion storage capacity. *J. Alloys Compd.* **2021**, *889*, 161542. [CrossRef]
52. Lu, H.; Li, J.; Lu, Y.; Chen, Y.A.; Xie, T.; Zhou, X.; Li, Q.; Pan, F. ZrO_2@Nb_2CT_x composite as the efficient catalyst for Mg/MgH_2 based reversible hydrogen storage material. *Int. J. Hydrogen Energy* **2022**, *47*, 38282–38294. [CrossRef]

53. Peng, C.; Wei, P.; Chen, X.; Zhang, Y.; Zhu, F.; Cao, Y.; Wang, H.; Yu, H.; Peng, F. A hydrothermal etching route to synthesis of 2D MXene (Ti_3C_2, Nb_2C): Enhanced exfoliation and improved adsorption performance. *Ceram. Int.* **2018**, *44*, 18886–18893. [CrossRef]
54. Dong, H.; Xiao, P.; Jin, N.; Wang, B.; Liu, Y.; Lin, Z. Molten Salt Derived Nb_2CT_x MXene Anode for Li-ion Batteries. *ChemElectroChem* **2021**, *8*, 957–962. [CrossRef]
55. Li, Y.; Shao, H.; Lin, Z.; Lu, J.; Liu, L.; Duployer, B.; Persson, P.O.A.; Eklund, P.; Hultman, L.; Li, M.; et al. A general Lewis acidic etching route for preparing MXenes with enhanced electrochemical performance in non-aqueous electrolyte. *Nat. Mater.* **2020**, *19*, 894–899. [CrossRef] [PubMed]
56. Song, M.; Pang, S.Y.; Guo, F.; Wong, M.C.; Hao, J. Fluoride-Free 2D Niobium Carbide MXenes as Stable and Biocompatible Nanoplatforms for Electrochemical Biosensors with Ultrahigh Sensitivity. *Adv. Sci.* **2020**, *7*, 2001546. [CrossRef]
57. Li, J.; Zeng, F.; El-Demellawi, J.K.; Lin, Q.; Xi, S.; Wu, J.; Tang, J.; Zhang, X.; Liu, X.; Tu, S. Nb2CTx MXene Cathode for High-Capacity Rechargeable Aluminum Batteries with Prolonged Cycle Lifetime. *ACS Appl. Mater. Interfaces* **2022**, *14*, 45254–45262. [CrossRef]
58. Liu, C.; Zhou, J.; Li, X.; Fang, Z.; Sun, R.; Yang, G.; Hou, W. Surface modification and in situ carbon intercalation of two-dimensional niobium carbide as promising electrode materials for potassium-ion batteries. *Chem. Eng. J.* **2022**, *431*, 133838. [CrossRef]
59. Nasrin, K.; Sudharshan, V.; Arunkumar, M.; Sathish, M. 2D/2D Nanoarchitectured Nb2C/Ti3C2 MXene Heterointerface for High-Energy Supercapacitors with Sustainable Life Cycle. *ACS Appl. Mater. Interfaces* **2022**, *14*, 21038–21049. [CrossRef] [PubMed]
60. Li, Z.; Dall'Agnese, Y.; Guo, J.; Huang, H.; Liang, X.; Xu, S. Flexible freestanding all-MXene hybrid films with enhanced capacitive performance for powering a flex sensor. *J. Mater. Chem. A* **2020**, *8*, 16649–16660. [CrossRef]
61. Zhao, Q.; Jiang, Y.; Duan, Z.; Yuan, Z.; Zha, J.; Wu, Z.; Huang, Q.; Zhou, Z.; Li, H.; He, F.; et al. A Nb2CTx/sodium alginate-based composite film with neuron-like network for self-powered humidity sensing. *Chem. Eng. J.* **2022**, *438*, 135588. [CrossRef]
62. Pang, S.Y.; Wong, Y.T.; Yuan, S.; Liu, Y.; Tsang, M.K.; Yang, Z.; Huang, H.; Wong, W.T.; Hao, J. Universal Strategy for HF-Free Facile and Rapid Synthesis of Two-dimensional MXenes as Multifunctional Energy Materials. *J. Am. Chem. Soc.* **2019**, *141*, 9610–9616. [CrossRef] [PubMed]
63. Liu, L.; Zschiesche, H.; Antonietti, M.; Gibilaro, M.; Chamelot, P.; Massot, L.; Rozier, P.; Taberna, P.L.; Simon, P. In Situ Synthesis of MXene with Tunable Morphology by Electrochemical Etching of MAX Phase Prepared in Molten Salt. *Adv. Energy Mater.* **2022**, *13*, 2203825. [CrossRef]
64. Huang, J.; Wang, M.; Zhang, X.; Tao, J.; Lu, L.; Qiao, G.; Liu, G. Anchoring of 2D CdS on Nb_2CT_x MXene nanosheets for boosting photocatalytic H_2 evolution. *J. Alloys Compd.* **2022**, *923*, 166256. [CrossRef]
65. Griffith, K.J.; Hope, M.A.; Reeves, P.J.; Anayee, M.; Gogotsi, Y.; Grey, C.P. Bulk and Surface Chemistry of the Niobium MAX and MXene Phases from Multinuclear Solid-State NMR Spectroscopy. *J. Am. Chem. Soc.* **2020**, *142*, 18924–18935. [CrossRef]
66. Li, Z.; Yu, L.; Milligan, C.; Ma, T.; Zhou, L.; Cui, Y.; Qi, Z.; Libretto, N.; Xu, B.; Luo, J.; et al. Two-dimensional transition metal carbides as supports for tuning the chemistry of catalytic nanoparticles. *Nat. Commun.* **2018**, *9*, 5258. [CrossRef]
67. Zhang, Y.; Xu, Y.; Gao, L.; Liu, X.; Fu, Y.; Ma, C.; Ge, Y.; Cao, R.; Zhang, X.; Al-Hartomy, O.A.; et al. MXene-based mixed-dimensional Schottky heterojunction towards self-powered flexible high-performance photodetector. *Mater. Today Energy* **2021**, *21*, 100479. [CrossRef]
68. Yang, Y.; Ting, C.S. Electronic structures and electron–phonon superconductivity of Nb_2C-based MXenes. *J. Phys. D-Appl. Phys.* **2020**, *53*, 485301. [CrossRef]
69. Zhu, J.; Chroneos, A.; Schwingenschlögl, U. Nb-based MXenes for Li-ion battery applications. *Phys. Status Solidi–Rapid. Res. Lett.* **2015**, *9*, 726–729. [CrossRef]
70. Seredych, M.; Shuck, C.E.; Pinto, D.; Alhabeb, M.; Precetti, E.; Deysher, G.; Anasori, B.; Kurra, N.; Gogotsi, Y. High-Temperature Behavior and Surface Chemistry of Carbide MXenes Studied by Thermal Analysis. *Chem. Mater.* **2019**, *31*, 3324–3332. [CrossRef]
71. Babar, Z.U.D.; Anwar, M.S.; Mumtaz, M.; Iqbal, M.; Zheng, R.-K.; Akinwande, D.; Rizwan, S. Peculiar magnetic behaviour and Meissner effect in two-dimensional layered Nb_2C MXene. *2D Mater.* **2020**, *7*, 035012. [CrossRef]
72. Din Babar, Z.U.; Fatheema, J.; Arif, N.; Anwar, M.S.; Gul, S.; Iqbal, M.; Rizwan, S. Magnetic phase transition from paramagnetic in Nb_2AlC-MAX to superconductivity-like diamagnetic in Nb_2C-MXene: An experimental and computational analysis. *RSC Adv.* **2020**, *10*, 25669–25678. [CrossRef]
73. Xu, G.; Wang, J.; Zhang, X.; Yang, Z. First principles study on geometric and electronic properties of two-dimensional Nb_2CT_x MXenes. *Chin. Phys. B* **2022**, *31*, 037304. [CrossRef]
74. Halim, J.; Persson, I.; Moon, E.J.; Kuhne, P.; Darakchieva, V.; Persson, P.O.A.; Eklund, P.; Rosen, J.; Barsoum, M.W. Electronic and optical characterization of 2D Ti_2C and Nb_2C (MXene) thin films. *J. Phys. Condens. Matter* **2019**, *31*, 165301. [CrossRef] [PubMed]
75. Palisaitis, J.; Persson, I.; Halim, J.; Rosen, J.; Persson, P.O.A. On the Structural Stability of MXene and the Role of Transition Metal Adatoms. *Nanoscale* **2018**, *10*, 10850–10855. [CrossRef] [PubMed]
76. Echols, I.J.; Holta, D.E.; Kotasthane, V.S.; Tan, Z.; Radovic, M.; Lutkenhaus, J.L.; Green, M.J. Oxidative Stability of $Nb_{n+1}C_nT_z$ MXenes. *J. Phys. Chem. C* **2021**, *125*, 13990–13996. [CrossRef]
77. Yuan, Z.; Wang, L.; Li, D.; Cao, J.; Han, W. Carbon-Reinforced Nb_2CT_x MXene/MoS_2 Nanosheets as a Superior Rate and High-Capacity Anode for Sodium-Ion Batteries. *ACS Nano* **2021**, *15*, 7439–7450. [CrossRef]
78. Qi, X.; Xu, W.; Tang, J.; Xu, Y.; Gao, Y.; Li, L.; Sasaki, S.-I.; Tamiaki, H.; Wang, X. Chlorophyll derivative intercalation into Nb_2C MXene for lithium-ion energy storage. *J. Mater. Sci.* **2022**, *57*, 9971–9979. [CrossRef]
79. Xu, H.; Fan, J.; Pang, D.; Zheng, Y.; Chen, G.; Du, F.; Gogotsi, Y.; Dall'Agnese, Y.; Gao, Y. Synergy of ferric vanadate and MXene for high performance Li- and Na-ion batteries. *Chem. Eng. J.* **2022**, *436*, 135012. [CrossRef]

80. Wu, Y.; Sun, Y.; Zheng, J.; Rong, J.; Li, H.; Niu, L. Exploring MXene-based materials for next-generation rechargeable batteries. *J. Phys. Energy* **2021**, *3*, 032009. [CrossRef]
81. Wu, Y.; Liu, D.; Qu, D.; Li, J.; Xie, Z.; Zhang, X.; Chen, H.; Tang, H. Porous oxygen-deficient $TiNb_2O_7$ spheres wrapped by MXene as high-rate and durable anodes for liquid and all-solid-state lithium-ion batteries. *Chem. Eng. J.* **2022**, *438*, 135328. [CrossRef]
82. Eglitis, R.I. Theoretical prediction of the 5 V rechargeable Li ion battery using $Li_2CoMn_3O_8$ as a cathode. *Phys. Scripta* **2015**, *90*, 094012. [CrossRef]
83. Li, M.-P.; Zhang, C.-B.; Li, Y.-D.; Zhang, D.-T.; Chang, C.-G.; Liu, M.-C. Insert organic molecules into Nb_2C layers through hydrogen bonds towards high-rate lithium ion storage. *Ionics* **2022**, *28*, 5099–5108. [CrossRef]
84. Wu, J.; Guan, Y.; Li, K.; Xie, Q.; Wang, Z.; Zhu, H.; Zhang, Q.; Li, X.; Yuan, G.; Cong, Y. 2D porous Nb_4N_5@Nb_2C heterojunctions for high-performance Li-ion batteries. *2D Mater.* **2021**, *9*, 015029. [CrossRef]
85. Li, A.; Wang, X.; Chen, J.; Dong, C.; Wang, D.; Mao, Z. Surface-Termination Groups' Tuning to Improve the Lithium-Ion-Storage Performance of $Ti_3C_2T_x$ MXene. *Coatings* **2022**, *12*, 1005. [CrossRef]
86. Peng, R.; Han, K.; Tang, K. MXene Surface Functional Groups Regulation: Enhancing Area Capacitance of Divalent Zinc Ion Micro-Supercapacitor. *J. Electrochem. Soc.* **2022**, *169*, 060523. [CrossRef]
87. Wang, K.; Jin, H.; Li, H.; Mao, Z.; Tang, L.; Huang, D.; Liao, J.-H.; Zhang, J. Role of surface functional groups to superconductivity in Nb_2C-MXene: Experiments and density functional theory calculations. *Surf. Interfaces* **2022**, *29*, 101711. [CrossRef]
88. Ma, P.; Fang, D.; Liu, Y.; Shang, Y.; Shi, Y.; Yang, H.Y. MXene-Based Materials for Electrochemical Sodium-Ion Storage. *Adv. Sci.* **2021**, *8*, e2003185. [CrossRef]
89. Aslam, M.K.; AlGarni, T.S.; Javed, M.S.; Shah, S.S.A.; Hussain, S.; Xu, M. 2D MXene Materials for Sodium Ion Batteries: A review on Energy Storage. *J. Energy Storage* **2021**, *37*, 102478. [CrossRef]
90. Zhang, W.; Zhang, F.; Ming, F.; Alshareef, H.N. Sodium-ion battery anodes: Status and future trends. *EnergyChem* **2019**, *1*, 100012. [CrossRef]
91. Lei, Y.-J.; Yan, Z.-C.; Lai, W.-H.; Chou, S.-L.; Wang, Y.-X.; Liu, H.-K.; Dou, S.-X. Tailoring MXene-Based Materials for Sodium-Ion Storage: Synthesis, Mechanisms, and Applications. *Electrochem. Energy Rev.* **2020**, *3*, 766–792. [CrossRef]
92. Zhang, W.; Jin, H.; Chen, G.; Zhang, J. Sandwich-like N-doped carbon nanotube@Nb_2C MXene composite for high performance alkali ion batteries. *Ceram. Int.* **2021**, *47*, 20610–20616. [CrossRef]
93. Xiao, J.; Wu, B.; Bai, L.; Ma, X.; Lu, H.; Yao, J.; Zhang, C.; Gao, H. Ag Nanoparticles decorated few-layer Nb_2CT_x nanosheets architectures with superior lithium/sodium-ion storage. *Electrochim. Acta* **2022**, *402*, 139566. [CrossRef]
94. Gao, H.; Guo, X.; Wang, S.; Zhang, F.; Liu, H.; Wang, G. Antimony-based nanomaterials for high-performance potassium-ion batteries. *EcoMat* **2020**, *2*, e12027. [CrossRef]
95. Aslam, M.K.; Xu, M. A Mini-Review: MXene composites for sodium/potassium-ion batteries. *Nanoscale* **2020**, *12*, 15993–16007. [CrossRef] [PubMed]
96. Hou, J.; Wang, Y.; Yang, W.; Wang, F.; Yang, D.; Zhang, Y.; Liang, F.; Li, X.; Zhang, Y.; Zhao, J. Application of MXenes in lithium-sulfur batteries. *Sci. China-Technol. Sci.* **2022**, *65*, 2259–2273. [CrossRef]
97. Tian, J.; Ji, G.; Han, X.; Xing, F.; Gao, Q. Advanced Nanostructured MXene-Based Materials for High Energy Density Lithium-Sulfur Batteries. *Int. J. Mol. Sci.* **2022**, *23*, 6329. [CrossRef]
98. Chen, D.; Wen, K.; Lv, W.; Wei, Z.; He, W. Separator Modification and Functionalization for Inhibiting the Shuttle Effect in Lithium-Sulfur Batteries. *Phys. Status Solidi–Rapid. Res. Lett.* **2018**, *12*, 1800249. [CrossRef]
99. Xiao, Z.; Li, Z.; Meng, X.; Wang, R. MXene-engineered lithium–sulfur batteries. *J. Mater. Chem. A* **2019**, *7*, 22730–22743. [CrossRef]
100. Song, C.; Zhang, W.; Jin, Q.; Zhang, Y.; Wang, X.; Bakenov, Z. In-situ constructed accordion-like Nb_2C/Nb_2O_5 heterostructure as efficient catalyzer towards high-performance lithium-sulfur batteries. *J. Power Sources* **2022**, *520*, 230902. [CrossRef]
101. Zong, H.; Hu, L.; Gong, S.; Yu, K.; Zhu, Z. Flower-petal-like Nb_2C MXene combined with MoS_2 as bifunctional catalysts towards enhanced lithium-sulfur batteries and hydrogen evolution. *Electrochim. Acta* **2022**, *404*, 139781. [CrossRef]
102. Li, X.; Ma, X.; Hou, Y.; Zhang, Z.; Lu, Y.; Huang, Z.; Liang, G.; Li, M.; Yang, Q.; Ma, J.; et al. Intrinsic voltage plateau of a Nb_2CT_x MXene cathode in an aqueous electrolyte induced by high-voltage scanning. *Joule* **2021**, *5*, 2993–3005. [CrossRef]
103. Shi, C.; Liu, Z.; Tian, Z.; Li, D.; Chen, Y.; Guo, L.; Wang, Y. Regulated layer spacing and functional surface group of MXene film by hexamethylenetetramine for high-performance supercapacitors. *Appl. Surf. Sci.* **2022**, *596*, 153632. [CrossRef]
104. Mohamed, S.G.; Hussain, I.; Sayed, M.S.; Shim, J.-J. One-step development of octahedron-like $CuCo_2O_4$@Carbon fibers for high-performance supercapacitors electrodes. *J. Alloys Compd.* **2020**, *842*, 155639. [CrossRef]
105. González, A.; Goikolea, E.; Barrena, J.A.; Mysyk, R. Review on supercapacitors: Technologies and materials. *Renew. Sust. Energ. Rev.* **2016**, *58*, 1189–1206. [CrossRef]
106. Augustyn, V.; Simon, P.; Dunn, B. Pseudocapacitive oxide materials for high-rate electrochemical energy storage. *Energy Environ. Sci.* **2014**, *7*, 1597–1614. [CrossRef]
107. Lu, M.; Han, W.; Li, H.; Zhang, W.; Zhang, B. There is plenty of space in the MXene layers: The confinement and fillings. *J. Energy Chem.* **2020**, *48*, 344–363. [CrossRef]
108. Sun, Y.; Yi, R.; Zhao, Y.; Liu, C.; Yuan, Y.; Geng, X.; Li, W.; Feng, Z.; Mitrovic, I.; Yang, L.; et al. Improved pseudocapacitances of supercapacitors based on electrodes of nitrogen-doped $Ti_3C_2T_x$ nanosheets with in-situ growth of carbon nanotubes. *J. Alloys Compd.* **2021**, *859*, 158347. [CrossRef]

109. Xiao, J.; Wen, J.; Zhao, J.; Ma, X.; Gao, H.; Zhang, X. A safe etching route to synthesize highly crystalline Nb_2CT_x MXene for high performance asymmetric supercapacitor applications. *Electrochim. Acta* **2020**, *337*, 135803. [CrossRef]
110. Shen, B.; Liao, X.; Zhang, X.; Ren, H.-T.; Lin, J.-H.; Lou, C.-W.; Li, T.-T. Synthesis of Nb_2C MXene-based 2D layered structure electrode material for high-performance battery-type supercapacitors. *Electrochim. Acta* **2022**, *413*, 140144. [CrossRef]
111. Liao, L.; Wu, B.; Kovalska, E.; Mazanek, V.; Vesely, M.; Marek, I.; Spejchalova, L.; Sofer, Z. The Role of Alkali Cation Intercalates on the Electrochemical Characteristics of Nb_2CT_x MXene for Energy Storage. *Chemistry* **2021**, *27*, 13235–13241. [CrossRef] [PubMed]
112. Qin, L.; Liu, Y.; Zhu, S.; Wu, D.; Wang, G.; Zhang, J.; Wang, Y.; Hou, L.; Yuan, C. Formation and operating mechanisms of single-crystalline perovskite $NaNbO_3$ nanocubes/few-layered Nb_2CT_x MXene hybrids towards Li-ion capacitors. *J. Mater. Chem. A* **2021**, *9*, 20405–20416. [CrossRef]
113. Zhao, W.; Jin, B.; Wang, L.; Ding, C.; Jiang, M.; Chen, T.; Bi, S.; Liu, S.; Zhao, Q. Ultrathin Ti_3C_2 nanowires derived from multi-layered bulks for high-performance hydrogen evolution reaction. *Chin. Chem. Lett.* **2022**, *33*, 557–561. [CrossRef]
114. Kang, Z.; Khan, M.A.; Gong, Y.; Javed, R.; Xu, Y.; Ye, D.; Zhao, H.; Zhang, J. Recent progress of MXenes and MXene-based nanomaterials for the electrocatalytic hydrogen evolution reaction. *J. Mater. Chem. A* **2021**, *9*, 6089–6108. [CrossRef]
115. Cui, C.; Cheng, R.; Zhang, H.; Zhang, C.; Ma, Y.; Shi, C.; Fan, B.; Wang, H.; Wang, X. Ultrastable MXene@Pt/SWCNTs' Nanocatalysts for Hydrogen Evolution Reaction. *Adv. Funct. Mater.* **2020**, *30*, 2000693. [CrossRef]
116. Han, M.; Yang, J.; Jiang, J.; Jing, R.; Ren, S.; Yan, C. Efficient tuning the electronic structure of N-doped Ti-based MXene to enhance hydrogen evolution reaction. *J. Colloid Interface Sci.* **2021**, *582*, 1099–1106. [CrossRef] [PubMed]
117. Fan, X.; Du, P.; Ma, X.; Wang, R.; Ma, J.; Wang, Y.; Fan, D.; Long, Y.; Deng, B.; Huang, K.; et al. Mechanochemical Synthesis of Pt/Nb_2CT_x MXene Composites for Enhanced Electrocatalytic Hydrogen Evolution. *Materials* **2021**, *14*, 2426. [CrossRef]
118. Zhang, S.; Zhuo, H.; Li, S.; Bao, Z.; Deng, S.; Zhuang, G.; Zhong, X.; Wei, Z.; Yao, Z.; Wang, J.-G. Effects of surface functionalization of mxene-based nanocatalysts on hydrogen evolution reaction performance. *Catal. Today* **2021**, *368*, 187–195. [CrossRef]
119. Makola, L.C.; Moeno, S.; Ouma, C.N.M.; Sharma, A.; Vo, D.-V.N.; Dlamini, L.N. Facile fabrication of a metal-free 2D–2D Nb_2CT_x@g-C_3N_4 MXene-based Schottky-heterojunction with the potential application in photocatalytic processes. *J. Alloys Compd.* **2022**, *916*, 165459. [CrossRef]
120. Tayyab, M.; Liu, Y.; Liu, Z.; Pan, L.; Xu, Z.; Yue, W.; Zhou, L.; Lei, J.; Zhang, J. One-pot in-situ hydrothermal synthesis of ternary $In_2S_3/Nb_2O_5/Nb_2C$ Schottky/S-scheme integrated heterojunction for efficient photocatalytic hydrogen production. *J. Colloid Interface Sci.* **2022**, *628*, 500–512. [CrossRef]
121. Xu, W.; Li, X.; Peng, C.; Yang, G.; Cao, Y.; Wang, H.; Peng, F.; Yu, H. One-pot synthesis of Ru/Nb_2O_5@Nb_2C ternary photocatalysts for water splitting by harnessing hydrothermal redox reactions. *Appl. Catal. B-Environ.* **2022**, *303*, 120910. [CrossRef]
122. Li, M.; Singh, R.; Soares, M.S.; Marques, C.; Zhang, B.; Kumar, S. Convex fiber-tapered seven core fiber-convex fiber (CTC) structure-based biosensor for creatinine detection in aquaculture. *Opt. Express* **2022**, *30*, 13898–13914. [CrossRef]
123. Kumar, A.N.; Pal, K. Amine-functionalized stable Nb_2CT_x MXene toward room temperature ultrasensitive NO_2 gas sensor. *Mater. Adv.* **2022**, *3*, 5151–5162. [CrossRef]
124. Li, W.; Miao, Y.; Zheng, Y.; Zhang, K.; Yao, J. Nb_2CT_x MXene Integrated Tapered Microfiber Based on Light-Controlled Light for Ultra-Sensitive and Wide-Range Hemoglobin Detection. *IEEE Sens. J.* **2022**, *22*, 11456–11462. [CrossRef]
125. Cui, C.; Guo, R.; Ren, E.; Xiao, H.; Zhou, M.; Lai, X.; Qin, Q.; Jiang, S.; Qin, W. MXene-based rGO/Nb_2CT_x/Fe_3O_4 composite for high absorption of electromagnetic wave. *Chem. Eng. J.* **2021**, *405*, 126626. [CrossRef]
126. Rajavel, K.; Yu, X.; Zhu, P.; Hu, Y.; Sun, R.; Wong, C. Investigation on the structural quality dependent electromagnetic interference shielding performance of few-layer and lamellar Nb_2CT_x MXene nanostructures. *J. Alloys Compd.* **2021**, *877*, 160235. [CrossRef]
127. Jin, Z.; Fang, Y.; Wang, X.; Xu, G.; Liu, M.; Wei, S.; Zhou, C.; Zhang, Y.; Xu, Y. Ultra-efficient electromagnetic wave absorption with ethanol-thermally treated two-dimensional Nb_2CT_x nanosheets. *J. Colloid Interface Sci.* **2019**, *537*, 306–315. [CrossRef]
128. Song, S.; Liu, J.; Zhou, C.; Jia, Q.; Luo, H.; Deng, L.; Wang, X. Nb_2O_5/Nb_2CT_x composites with different morphologies through oxidation of Nb_2CT_x MXene for high-performance microwave absorption. *J. Alloys Compd.* **2020**, *843*, 155713. [CrossRef]
129. Zhang, J.; Huang, C.; Sun, Y.; Yu, H. Amino-Functionalized Niobium-Carbide MXene Serving as Electron Transport Layer and Perovskite Additive for the Preparation of High-Performance and Stable Methylammonium-Free Perovskite Solar Cells. *Adv. Funct. Mater.* **2022**, *32*, 2113367. [CrossRef]
130. Chu, K.; Li, X.; Li, Q.; Guo, Y.; Zhang, H. Synergistic Enhancement of Electrocatalytic Nitrogen Reduction Over Boron Nitride Quantum Dots Decorated Nb_2CT_x -MXene. *Small* **2021**, *17*, e2102363. [CrossRef]
131. Xia, W.; Cheng, H.; Zhou, S.; Yu, N.; Hu, H. Synergy of copper Selenide/MXenes composite with enhanced solar-driven water evaporation and seawater desalination. *J. Colloid Interface Sci.* **2022**, *625*, 289–296. [CrossRef] [PubMed]
132. Huang, X.; Zhang, W.; Liu, W.; Zhang, J.; Song, M.; Zhang, C.; Zhang, J.; Wang, D. Nb_2CT_x MXenes functionalized Co−NC enhancing electrochemical H_2O_2 production for organics degradation. *Appl. Catal. B-Environ.* **2022**, *317*, 121737. [CrossRef]
133. Li, C.; Liang, L.; Liu, X.; Cao, N.; Shao, Q.; Zou, P.; Zang, X. A lean-zinc anode battery based on metal–organic framework-derived carbon. *Carbon Energy* **2022**. [CrossRef]